



High-efficiency V-Mediated Bi₂MoO₆ photocatalyst for PMS activation: Modulation of energy band structure and enhancement of surface reaction

Jun Yang^{a,i,1}, Taiping Xie^{b,c,*}, Yuhang Mei^{g,h,1}, Junyu Chen^b, Hao Sun^d, Shan Feng^e, Yu Zhang^b, Ying Zhao^b, Jiankang Wang^{b,**}, Xiaoqing Li^f, Jiahong He^a, Houyang Chen^{g,h,***}

^a Chongqing Key Laboratory of Environmental Materials & Remediation Technologies, College of Chemistry and Environmental Engineering, Chongqing University of Arts and Sciences, Chongqing 402160, China

^b School of Materials Science and Engineering, Yangtze Normal University, Chongqing 408100, China

^c Chongqing Preschool Education College, Chongqing 404047, China

^d School of Environmental and Chemical Engineering, Chongqing Three Gorges University, Wanzhou 404100, China

^e School of Mining and Civil Engineering, Liupanshui Normal University, Liupanshui 553004, China

^f Department of Chemical Engineering, Chongqing Chemical Industry Vocational College, Chongqing 401228, China

^g Chongqing Institute of Green and Intelligent Technology, Chinese Academy of Sciences, Chongqing 400714, China

^h Chongqing School, University of Chinese Academy of Sciences, Chongqing 400044, China

ⁱ School of Resources and Safety Engineering, Chongqing University, Chongqing 402160, China

ARTICLE INFO

Keywords:

Bi₂MoO₆

V doping

Photocatalytic activation PMS

Sulfapyridine degradation

ABSTRACT

High photocorrosion and poor reaction efficiency of Bi₂MoO₆ greatly hampered its wide application in wastewater treatment. Herein, V doped Bi₂MoO₆ was prepared by hydrothermal-subsequent annealing strategy for the refractory sulfapyridine abatement through visible-light-driven photocatalytic activation of peroxymonosulfate (PMS). The degradation results revealed V-doped Bi₂MoO₆ could achieved 100% sulfapyridine removal after 20 min over Bi₂MoO₆/PMS/Vis system, much higher than Bi₂MoO₆/PMS/Vis system. Experimental and theoretical calculations indicated that the V doping not only changed the energy band structure of Bi₂MoO₆ and promoted the separation of photogenerated charges as well as improved the adsorption energy of peroxymonosulfate (PMS), H₂O and dissolved oxygen on the catalyst surface, but also provided additional PMS activation pathway through V⁵⁺/V⁴⁺ redox cycles, finally contributed to enhanced sulfapyridine degradation performance in Bi₂MoO₆/PMS/Vis system. Our work provides insight into designing highly efficient photocatalyst as a promising PMS activator for environmental application.

1. Introduction

The real danger of antibiotic overuse and antibiotic pollution was that it increased bacterial resistance and bred superbugs [1,2]. The residual and prolonged presence of persistent sulfapyridine in the environment not only bred resistant bacteria, but also caused damage to the human liver and central nervous system through the food chain [3,4]. Therefore, it was imperative to study the complete degradation of sulfapyridine antibiotics in wastewater.

Conventional methods such as biodegradation and chemisorption no longer met the needs of practical applications. Advanced oxidation

technologies for organic wastewater treatment, such as photocatalysis, had attracted much attention and continued research due to the advantages of inexhaustible solar energy as an energy source and environmental friendliness. However, for a single photocatalytic degradation reaction, the reaction efficiency had become a bottleneck problem [5]. This was attributed to the yield of ·OH, the basic physical properties of ·OH such as oxidation potential and pH adaptation, etc. The anthraquinone-2-sulfonate (AQ2S)/graphene, Ag₃PO₄/g-C₃N₄, and decatungstate were used as photocatalysts to degrade sulfapyridine under visible light [6–8]. The reaction time of these three reaction systems exceeded 2 h, but failed to achieve complete degradation or

* Corresponding author at: School of Materials Science and Engineering, Yangtze Normal University, Chongqing 408100, China.

** Corresponding author.

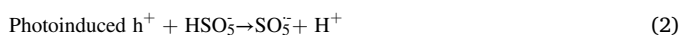
*** Corresponding author at: Chongqing Institute of Green and Intelligent Technology, Chinese Academy of Sciences, Chongqing 400714, China.

E-mail addresses: deartaiping@163.com (T. Xie), wjkwjk074478@163.com (J. Wang), chenhouyang@cigit.ac.cn (H. Chen).

¹ The authors have contributed equally to this work.

even degradation efficiencies below 80%. It was known that $\text{SO}_4^{\cdot-}$ had a higher oxidation potential, a wider range of pH adaptability, a longer life span, etc. If both $\cdot\text{OH}$ and $\text{SO}_4^{\cdot-}$ could be produced in a photocatalytic system, it was expected to overcome the bottleneck problem of reaction efficiency. However, we used two catalysts, $\text{Cu}_{0.76}\text{Co}_{2.24}\text{O}_4/\text{SBA-15}$ and $\text{Cu}_{0.2}\text{Ni}_{0.8}\text{O}/\text{SBA-15}$ to activate PMS to produce a variety of free radicals, but it still took 90 min to completely degrade sulfapyridine [9,10]. Afterwards, our studies confirmed that photocatalytic activation of PMS could produce multiple active species coexistence systems. Therefore, the construction of a $\text{SO}_4^{\cdot-}$ synergistic photocatalytic advanced oxidation process, namely photocatalytic activation of PMS should be capable of significantly improving the reaction efficiency.

Many studies suggested that PMS could be activated by photoinduced electrons and holes to generate $\text{SO}_4^{\cdot-}$ and $\text{SO}_5^{\cdot-}$, respectively (Eqs. 1–2) [11,12]. Besides, many reports, including our own, had indicated that oxygen vacancies with unpaired electrons could provide electrons to activate PMS [13–15] and produce both $\text{SO}_4^{\cdot-}$ and $\cdot\text{OH}$ (Eqs. 3–4). Therefore, it was easy to think that photocatalytic materials with oxygen defects might have efficient catalytic properties for PMS activation.



Bismuth-based photocatalysts, such as BiOX ($X = \text{Cl}, \text{I}, \text{Br}$), BiPO_4 , BiVO_4 , Bi_2WO_6 , and Bi_2MoO_6 , possessed a certain separation ability of photogenerated charge due to a special intrinsic layer structure that caused the generation of a built-in electric field [16,17]. More interestingly, the oxygen defect content of these bismuth-based photocatalysts increased with the time of light exposure. It could be concluded that the bismuth-based photocatalytic material had an efficient activation capacity for PMS. However, among bismuth-based photocatalytic materials, Bi_2MoO_6 could absorb visible light due to its appropriate band-gap (about 2.5–2.7) [18,19]. However, its practical application was hampered by high photocorrosion and poor efficiency stemming from high photogenerated carrier recombination. It was shown that the doping of Cu, Fe, W, In and lanthanide elements to modify Bi_2MoO_6 to improve its photocatalytic activity [20–23]. The essence was that the introduction of 3d or 4f orbital electrons altered the energy band structure of Bi_2MoO_6 , which enhanced the photo-response intensity and thus the photocatalytic activity. Unfortunately, these elements possessed only a slight narrowing effect on the band gap width of Bi_2MoO_6 , and the reaction efficiency of the modified Bi_2MoO_6 still needs to be further upgraded in the corresponding application areas [21–24]. Existing research on V-doped modified SrTiO_3 , TaON , $\text{g-C}_3\text{N}_4$, CaTiO_3 [25–29] found that the introduction of V as an electron trap captured photogenerated electrons to improve the separation of photogenerated charges; the introduced V could form doped energy levels under the conduction band and narrow the band gap; the multi-valence V element provided donor energy level and changed the electronic structure.

In this work, Bi_2MoO_6 was selected as the photocatalyst, which was modified by doping with the versatile V element. The initial intention was that the V introduction would further improve the efficiency of photogenerated charge separation. Unexpectedly, the V introduction has achieved a multi-functional effect. That was, the V introduction changed the energy band structure and surface properties, enhanced the surface reaction, and increased the content of oxygen vacancies. In addition, the multivalent V ($\text{V}^{5+}/\text{V}^{4+}$ redox cycles) on the surface of the catalyst could activate the PMS directly. These changes have a synergistic effect to enhance the catalytic activity of Bi_2MoO_6 . Hence, the refractory sulfapyridine could be completely degraded over $\text{V-Bi}_2\text{MoO}_6/\text{PMS}$ after 20 min reaction under visible light. The quenching experiments and EPR tests indicated that photoinduced h^+ , $\cdot\text{OH}$, and $\text{O}_2^{\cdot-}$ played

dominant role in sulfapyridine degradation. Then, based on the LC-MS test results, the degradation pathway of sulfapyridine was proposed. Meanwhile, the toxicity evaluation of the intermediates revealed that the toxicity of degradation intermediates was much lower than that of sulfapyridine itself. In addition, a large number of experiments, such as UV-DRS, EIS, $i-t$, PL tests, combined with theoretical calculations, had investigated the enhancement mechanism of catalytic activity.

2. Experimental section

2.1. Chemicals and reagents

Peroxymonosulfate (PMS; $2\text{KHSO}_5 \cdot \text{KHSO}_4 \cdot \text{K}_2\text{SO}_4$), bismuth nitrate pentahydrate ($\text{Bi}(\text{NO}_3)_3 \cdot 5\text{H}_2\text{O}$), sodium vanadate (NH_4VO_3) were purchased from Aladdin Co., China. Sodium molybdate dihydrate ($\text{Na}_2\text{MoO}_4 \cdot 2\text{H}_2\text{O}$), sodium dodecyl benzene sulfonate (SDBS), sodium hydroxide (NaOH), sulfuric acid (H_2SO_4), nitric acid (HNO_3), citric acid, methanol (MeOH), tert-butyl alcohol (TBA), benzoquinone ($p\text{-BQ}$), L-histidine, EDTA-2Na, sulfapyridine, rhodamine 6B (RhB) were purchased from Sinopharm Chemical Reagent Co., Ltd. All reagents were analytical grade and were used as received without further purification. Deionized water was used throughout this work.

2.2. Preparation of catalyst

0.5 mmol of $\text{Bi}(\text{NO}_3)_3 \cdot 5\text{H}_2\text{O}$ was dissolved in 60 mL of deionized water. Then 1.5 mmol of sodium dodecyl benzene sulfonate (SDBS) was added under stirring conditions and the homogeneous solution was formed by continuous stirring for 1 h. 0.5 mmol NH_4VO_3 was dissolved in 60 mL of water and stirred for 30 min to form a homogeneous solution. Finally, the above two homogeneous solutions were mixed and stirred for 30 min to form a stable precursor solution A. 6 mmol $\text{Bi}(\text{NO}_3)_3 \cdot 5\text{H}_2\text{O}$ and 3 mmol $\text{Na}_2\text{MoO}_4 \cdot 2\text{H}_2\text{O}$ were dissolved in 60 mL, 1 mol/L HNO_3 and NaOH solution, respectively. 6 mmol citric acid was added to the formed $\text{Bi}(\text{NO}_3)_3$ solution. The $\text{Bi}(\text{NO}_3)_3$ solution mixed with citric acid was then mixed with Na_2MoO_4 solution and stirred for 30 min to form a stable precursor solution B. The pH of the precursor solutions A and B was adjusted to 7 and allowed to stand for 2 h. Then the two precursor solutions were mixed and transferred to a 150 mL hydrothermal reactor and reacted at 160°C for 24 h. After the reactor cooled, the solution was filtered, and the filter residue was dried in a vacuum oven at 60°C for 6 h. Then the sample was roasted in a muffle furnace at 230°C for 2 h. By adjusting the ratio of NH_4VO_3 , catalysts with different amounts of V-doping (9 mol%, 11 mol%, 14 mol%, 17 mol% and 19 mol%) could be prepared. The pure Bi_2MoO_6 was prepared by a similar procedure without precursor solution A.

2.3. Materials Characterization

The crystal structure and phase of the catalysts were analyzed by X-ray diffraction (XRD, Shimadzu 6100) using $\text{Cu K}\alpha$ X-ray radiation ($\lambda = 1.5432 \text{ \AA}$) in a 2θ range of $10^\circ \sim 80^\circ$. The chemical bonds on the surface of the catalysts were studied by Fourier transform infrared spectroscopy (Thermo Fisher, Nicolet IS5, USA) using KBr powder-pressed pellets. The morphologies and elemental distributions were characterized by field emission scanning electron microscopy (SEM, Thermo Fisher Quattro S) at 3 kV acceleration voltage and transmission electron microscopy (TEM, JEM 2100 F, JEOL, Japan) equipped with energy dispersive spectroscopy (EDS). The elemental composition of the catalysts, corresponding to the valence state, and the valence band energy were analyzed by X-ray photoelectron spectroscopy (XPS, Thermo Scientific Escalab 250Xi) with $\text{Al-K}\alpha$ ($h\nu = 1486.6 \text{ eV}$) as the radiation source. The C 1s peak (binding energy = 284.8 eV) was used as a calibration standard. The optical properties of the samples were examined using a UV-3600 plus ultraviolet-visible diffuse reflectance spectrophotometer (UV-vis DRS, Shimadzu, Japan). Meanwhile, the photoluminescence

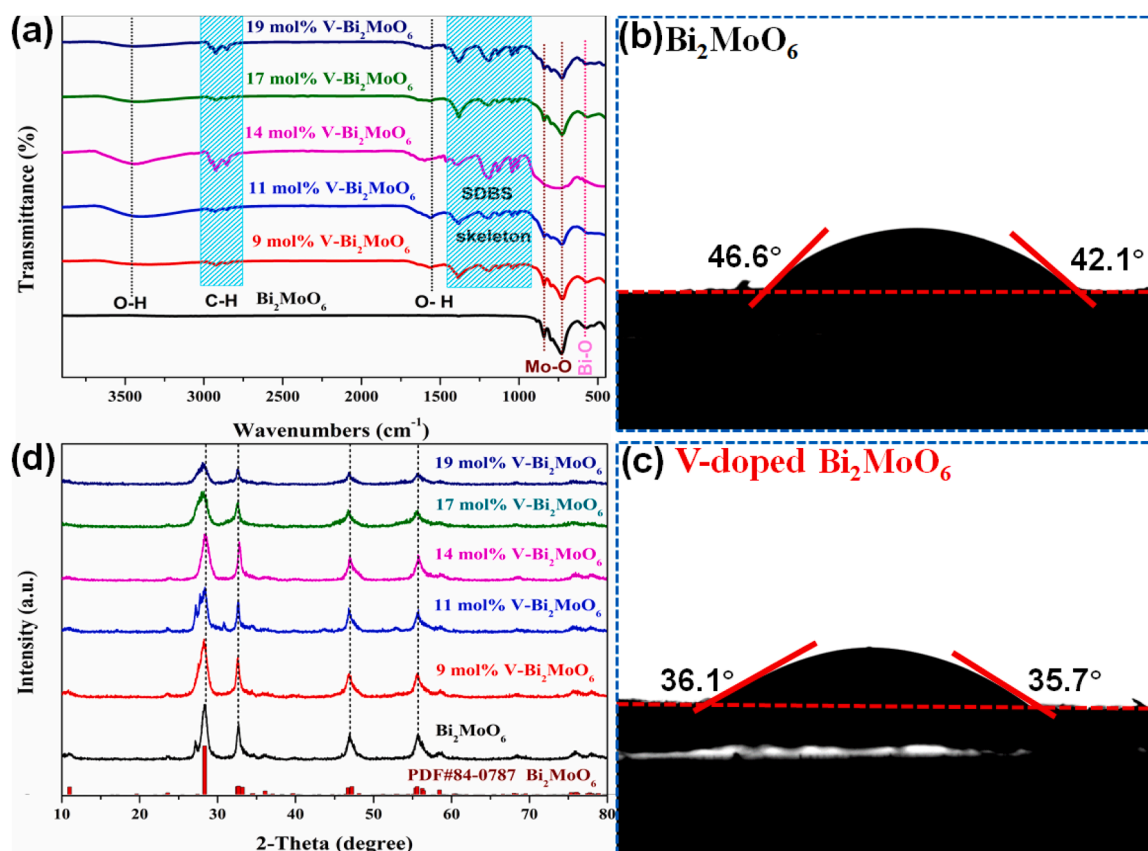


Fig. 1. FTIR (a) patterns of samples; water-contact angles of Bi₂MoO₆ (b) and 14 mol% V-doped Bi₂MoO₆ (c) surfaces; XRD (d) patterns of samples.

emission spectra were recorded using a full-function steady/transient fluorescence spectrometer (PL, FLS1000, Edinburgh UK). Other characterization details such as specific surface area, pore structure and contact angle are presented in [Text S1 of the Support Information](#). In the meantime, the detail information about electrochemical and photoelectrochemical tests are provided in [Text S2 of the Support Information](#).

2.4. Degradation procedures

Here, all the degradation experiments were performed in duplicate to ensure the accuracy of all results. The reaction process to optimize the amount of V doping by the degradation reaction of RhB and the degradation reaction process of sulfapyridine used the same photocatalytic reactor to ensure that the optical coefficients of the reaction apparatus did not affect the experimental results [30,31]. Batch experiments were carried out in a photocatalytic reactor with mechanical stirring, and the temperature of the solution was controlled at 20 °C by flowing condensate water. In each experiment, the desired catalyst dose was added to the reaction vessel containing 150 mL sulfapyridine solution and then mechanically stirred for 30 min to reach adsorption-desorption equilibrium. Then, a certain dose of PMS was added to the solution. Subsequently, a 300 W xenon lamp with an ultraviolet cutoff filter was turned on to simulate visible-light irradiation ($\lambda > 420$ nm and light intensity of 700 mW·cm⁻², measured by a light meter). The distance between the xenon lamp and the reaction vessel was always maintained at 15 cm. At the given irradiation time intervals, 3 mL of the reaction solution was sampled from the middle of the reactor. The sulfapyridine concentration was measured using ultra-high-performance liquid chromatograph (UPLC, Waters). The detailed experimental parameters are shown in [Text S3 of the Support Information](#).

By convention, C/C_0 represents the photodegradation rate, where C_0 is the concentration of the initial solution and C is the concentration of the reaction solution after different reaction times. $(1-C/C_0) \times 100\%$ was used to calculate the degradation efficiency. $\ln(C_0/C) = k \cdot t$ was used to fit and calculate the reaction rate constant (k).

It should be noted that the degradation procedure for RhB was the same as above, except that PMS was not added. The same reaction vessel was used for the degradation of rhodamine B and sulfapyridine.

2.5. Theoretical calculation

We have used first principles [32,33] to perform all density functional theory (DFT) calculations within the generalized gradient approximation (GGA) using the Perdew-Burke-Ernzerhof (PBE) [34] formulation. We chose the Projected Augmented Wave (PAW) potentials [35,36] to describe the ionic cores and account for valence electrons using a plane wave basis set with a kinetic energy cutoff of 450 eV. Partial occupancies of the Kohn-Sham orbitals were allowed using the Gaussian smearing method and a width of 0.05 eV. The electronic energy was considered self-consistent if the energy change was less than 10^{-4} eV. A geometry optimization was considered convergent if the energy change was less than $0.05 \text{ eV} \cdot \text{\AA}^{-1}$. The U correction is used for Mo atoms ($U=7.7 \text{ eV}$, $J=0.7 \text{ eV}$). All calculation work was carried out by adopting Vienna ab initio Simulation Package (VASP) [32]. Bi₂MoO₆ (131) surface model was built with 32 Bi atoms, 16 Mo atoms and 96 O atoms. In the V-doped Bi₂MoO₆ surface model, a Mo atom was replaced with a V atom and an adjacent O atom was then removed, creating an O vacancy. The vacuum distance in a direction perpendicular to the plane of the structure is 20 Å for the surfaces. The Brillouin zone integration is performed using $2 \times 2 \times 1$ Monkhorst-Pack k-point sampling for a structure. Finally, the adsorption energies (E_{ads}) were calculated as $E_{\text{ads}} = E_{\text{ad/sub}} - E_{\text{ad}} - E_{\text{sub}}$, where $E_{\text{ad/sub}}$, E_{ad} and E_{sub} are the total

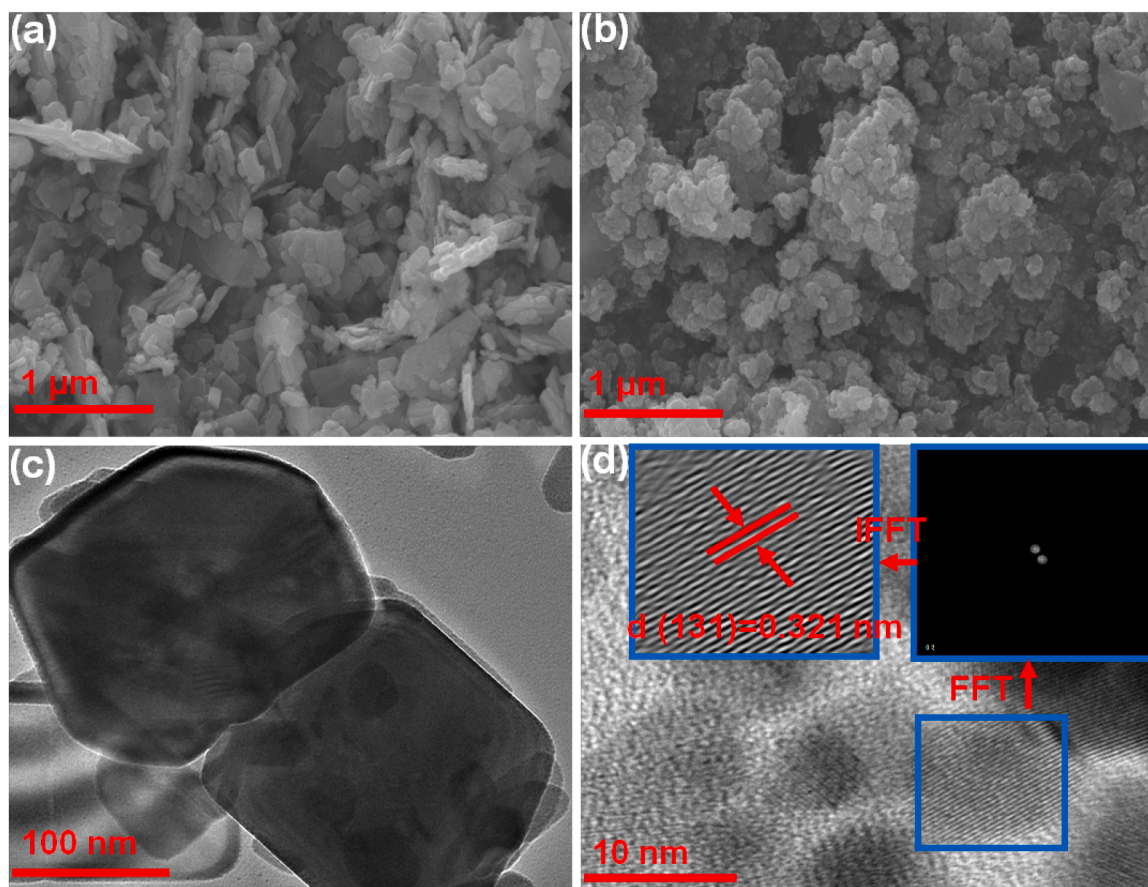


Fig. 2. SEM images of Bi_2MoO_6 (a) and V-doped Bi_2MoO_6 (b), TME (c) and HRTEM (d) images of V-doped Bi_2MoO_6 .

energies of the optimized adsorbate/substrate system, the adsorbate in the structure, and the clean substrate, respectively.

In addition, the toxicity assessment method of sulfapyridine and its degradation intermediates using Toxicity Estimation Software Tool (T.E.S.T) is shown in the Text S6 of the Supporting Information. The calculation method for sulfapyridine molecule structure and FuKu index was fully referenced from previous reports [1,37].

3. Results and discussion

As a classical probe reaction, the photocatalytic degradation of RhB was used for the optimization of the V-doping ratio. As shown in Fig. S1a, Bi_2MoO_6 with 14 mol% V-doping had the largest adsorption capacity for RhB, about 48%, which facilitated the subsequent degradation reaction. The adsorption of RhB over all the catalyst samples, 14 mol% V-doped Bi_2MoO_6 showed the highest adsorption of RhB, indicating that it may have the largest specific surface area. Thus, RhB degradation reaction over 14 mol% V-doped Bi_2MoO_6 possessed a high reaction kinetics than over other V-doping ratio. The higher adsorption of RhB on the catalyst during the pH optimization process (Fig. S1b) might be due to the different charging conditions and potentials of the RhB molecular structure and the catalyst surface under different pH conditions. This adsorption process is a complex physical process [38–40] that needs to be investigated in depth in following work. Under optimal reaction conditions, pH=5 (Fig. S1b) and 0.11 g of 14 mol% V-doped Bi_2MoO_6 (Fig. S1c), the RhB degradation efficiency could reach 91.0% after 1 h of reaction. However, under the same conditions, pure Bi_2MoO_6 could hardly degrade RhB. Two preliminary conclusions could be drawn from the experimental results. On the one hand, the molecular structure of RhB was very stable and the aromatic ring in RhB was not easily opened by OH^\cdot ; on the other hand, the recombination of

photogenerated carriers was severe in the pure Bi_2MoO_6 system [19], while V-doping promoted the separation of photogenerated charges and thus improved the catalytic activity. In the subsequent studies, 14 mol% V-doped Bi_2MoO_6 was used for many characterization tests. Therefore, 14 mol% V-doped Bi_2MoO_6 was abbreviated as V-doped Bi_2MoO_6 .

3.1. Chemical bond, phase, morphology, and elemental composition

FTIR spectroscopy can provide a great deal of information about chemical bonds. As shown in Fig. 1a, the characteristic absorption peaks at 2926.7 cm^{-1} and 2852.0 cm^{-1} .

were due to the stretching vibration of the C-H bonds stemming from SDBS molecular.

Many absorption peaks in the range of $914.6\text{ cm}^{-1} \sim 1457.4\text{ cm}^{-1}$ could be attributed to the molecular backbone of SDBS. In the preparation of pure Bi_2MoO_6 , no SDBS was added, so the above absorption peaks were not present in the FTIR spectrum of Bi_2MoO_6 .

The characteristic absorption peaks at 839.9 cm^{-1} and 728.2 cm^{-1} were present in the spectra of all samples, which were attributed to the stretching vibration of the Mo-O bond [41,42]. Similarly, absorption peak at 547.5 cm^{-1} was ascribed to the stretching vibration of Bi-O bond [42,43]. In addition, the absorption peaks at 3458.9 cm^{-1} and 1553.5 cm^{-1} were assigned to the stretching vibration of O-H bond originated from adsorbed water [44,45]. In general, the greater the intensity of these two absorption peaks, the more the catalyst absorbed water, i.e., the more hydrophilic the catalysts. Therefore, the hydrophilicity of the V-doped Bi_2MoO_6 was stronger than that of the pure Bi_2MoO_6 . The high hydrophilicity promoted sufficient water-photocatalyst contact, which in turn increased the probability of surface reaction, facilitating the photocatalytic reaction to generate OH^\cdot [46]. To verify the hydrophilicity of the catalysts, we investigated the

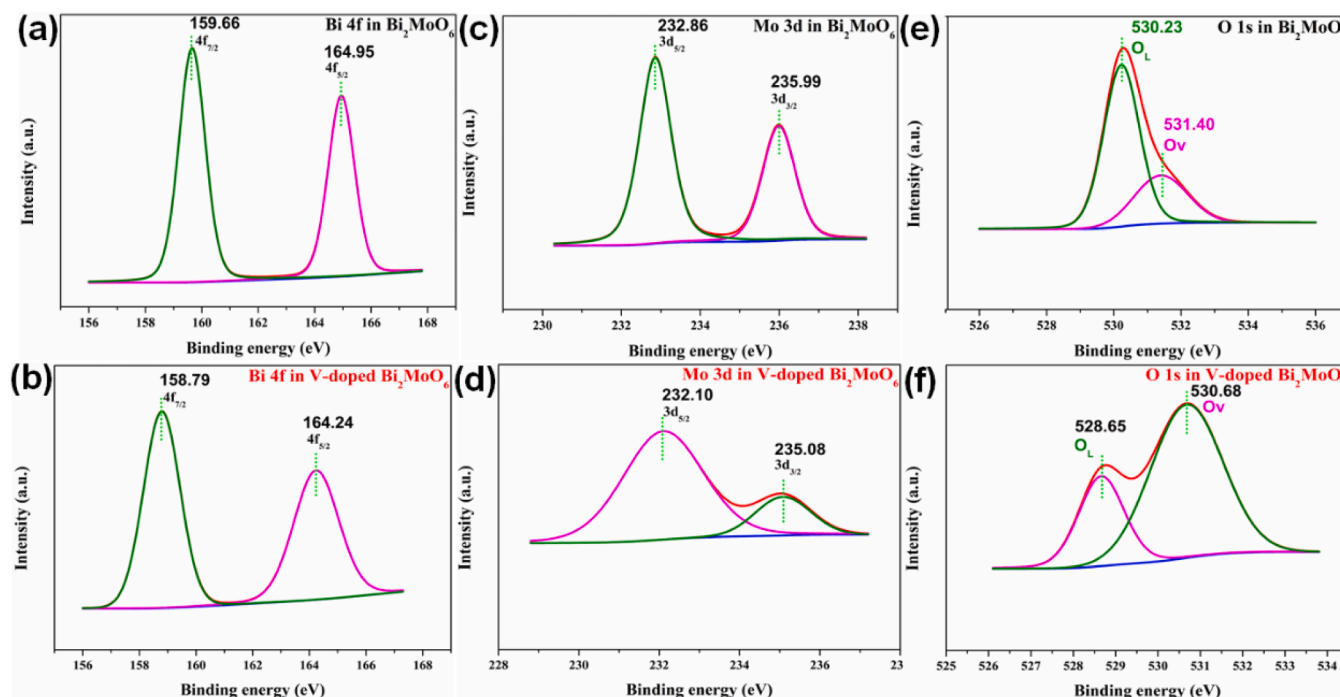


Fig. 3. XPS total survey of samples (a, b) and high-resolution XPS of corresponding elements.

ability of the catalyst surface to adsorb water through the water contact angle (Fig. 1b, c). After 1 s of contact with water droplets, the average contact angle of V-doped Bi_2MoO_6 was only 35.9° , while the contact angle of Bi_2MoO_6 was 44.4° . The results were consistent with FTIR analysis.

The diffraction peaks at 28.4° , 32.6° , 47.1° , and 55.5° corresponded to the (131), (200), (260), and (331) lattice planes, which were characteristic diffraction peaks of Bi_2MoO_6 [18,43]. Each V-doped sample had corresponding characteristic peaks at these 2θ positions, which indicated that the V-doping did not alter crystal structure of Bi_2MoO_6 (Fig. 1d). Meanwhile, there were no other impurity peaks, revealing that no new phases created by the V-doping. The 2θ angle of the diffraction peak of the (131) plane became smaller and smaller with increasing V-doping dosage, which was due to that V atoms caused lattice distortion, resulting in an increase in crystal plane spacing and then a decrease in the 2θ angle of the diffraction peak of the (131) plane. With increasing V-doping, there was an irregular change in grain size, although crystallinity did not change (Fig. S2). The 14 mol% V-doped Bi_2MoO_6 sample possessed the smallest grain size, about 8.5 nm, which was smaller than pure Bi_2MoO_6 (about 13.4 nm). Therefore, the specific surface area of Bi_2MoO_6 is increased by the appropriate amount of V-doping. To verify the above inference, specific surface area and pore structure characteristics were analyzed (Fig. S3). The specific surface area of pure Bi_2MoO_6 and V-doped Bi_2MoO_6 were $7.179 \text{ m}^2/\text{g}$ and $39.215 \text{ m}^2/\text{g}$, respectively (Fig. S3a). The average pore size distribution of pure Bi_2MoO_6 and V-doped Bi_2MoO_6 were 13.75 nm and 9.55 nm (Fig. S3b), respectively. These results were consistent with the above inference. In addition, the pure Bi_2MoO_6 and V-doped Bi_2MoO_6 samples could be identified as a mesoporous material because the average pore size distribution of the sample was between 2 nm and 50 nm.

SEM images of pure Bi_2MoO_6 (Fig. 2a) and V-doped Bi_2MoO_6 (Fig. 2b) clearly demonstrated their lamellar structures. Besides, TEM image of V-doped Bi_2MoO_6 further confirmed its lamellar morphology (Fig. 2c). In addition, the particle size of V-doped Bi_2MoO_6 crystals was obviously smaller than that of pure Bi_2MoO_6 crystals, indicating that the introduction of V could reduce the particle size of the crystals and increase the specific surface area, which was consistent with the conclusions of the above XRD (Fig. S2) and specific surface area analysis

(Fig. S3). The lattice spacing was calculated by the lattice Fourier and inverse Fourier transforms (Fig. 2d). The lattice spacing of 0.321 nm corresponded to (131) crystal surface [18,19], which further confirmed that the Bi_2MoO_6 sample was successfully prepared. But the lattice spacing of (131) crystal surface of V-doped Bi_2MoO_6 (0.321 nm) was indeed larger than that of Bi_2MoO_6 (0.316 nm). This result also further verified that V-doping caused an increase in the d-spacing of the crystal plane, which was consistent with the conclusion from the XRD analysis. Because the atomic radius of V, Bi, and Mo were 1.92 Å, 1.63 Å, and 2.01 Å, respectively. The introduction of V increased the d-spacing of the crystal plane, indicating that V was doped into the Bi_2MoO_6 system rather than replacing Bi or Mo in the Bi_2MoO_6 system. EDS elements mapping presented the desired Bi, Mo, V, and O elements and corresponding uniform distribution (Fig. S4). The total XPS spectra of pure Bi_2MoO_6 (Fig. S5a) and V-doped Bi_2MoO_6 (Fig. S5b) also further confirmed the presence of the desired elements. In fact, these results could also prove that the V-doped Bi_2MoO_6 was successfully prepared.

The high-resolution XPS of Bi 4f, Mo 3d, O 1s, and V 2p were analyzed to clarify their chemical state. The binding energies at 158.7–158.9 eV and 164.0–164.3 eV were attributable to Bi 4f_{7/2} and Bi 4f_{5/2} states [47,48], respectively (Fig. 3a, b). The fitted peaks at 231.9–233.0 eV and 235.0–236.0 eV were assignable to Mo 3d_{5/2} and Mo 3d_{3/2} states [48,49], respectively (Fig. 3c, d), indicating the presence of Mo^{5+} and Mo^{6+} [50]. The O 1s spectrum centered at 528.6–530.5 eV and 530.5–531.7 eV could be ascribable to lattice oxygen and oxygen vacancy [15,51,52], respectively (Fig. 3e, f). The binding energies of Bi 4f, Mo 3d, and O 1s in the V-doped Bi_2MoO_6 were lower than those in the pure Bi_2MoO_6 , which was due to that the electronegativity of the doped V (1.6) was lower than that of Bi (1.9), Mo (1.8), and O (3.5). The electrons at the top of the V valence band were attracted away through the formed oxygen bridge bonds (Bi/Mo-O-V). On the one side, the results confirmed that V-doped Bi_2MoO_6 was successfully prepared once again. On the other side, the V would be present in the state of high valence. The fitted peaks at 515.6 eV and 522.9 eV belonged to V 2p_{3/2} and V 2p_{1/2} (Fig. S6), further indicating the presence of V^{5+} [47,52]. Compared with pure Bi_2MoO_6 , V-doped Bi_2MoO_6 possessed more oxygen vacancies (Fig. 3e, f), signifying that V-doping increased oxygen vacancies in Bi_2MoO_6 . The results of solid

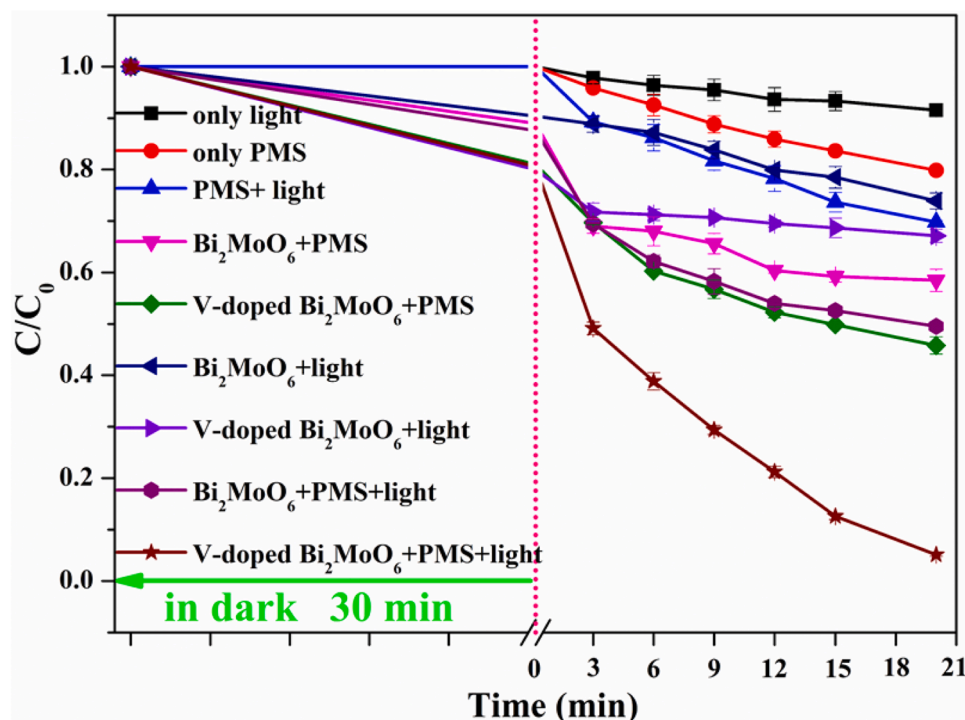


Fig. 4. The sulfapyridine degradation efficiency under different catalytic systems. Conditions: [sulfapyridine] = 0.05 mmol/L, [catalyst] = 0.50 g/L, [PMS] = 0.3 g/L, pH = 3.

EPR test for oxygen vacancies (Fig. S7) were in accordance with XPS analysis.

3.2. Sulfapyridine degradation

The initial concentration of the sulfapyridine solution, catalyst dosage, PMS dosage, and the pH of the reaction solution were optimized. The optimal reaction conditions were 0.05 mmol/L for the initial concentration of sulfapyridine, 0.50 g/L for the amount of catalyst, 0.3 g/L for the amount of PMS, and 3.0 g/L for the pH of the reaction solution (Fig. S8). It should be noted that the pH of the reaction solution was adjusted after the addition of PMS to the sulfapyridine solution because of the strong influence of PMS on the pH of the sulfapyridine solution and the influence of the pH of the reaction solution on the decomposition of PMS.

A variety of experiments have been carried out to compare the catalytic ability of different catalytic systems to degrade sulfapyridine. As shown in Figs. 4, 8.0% degradation efficiency under only visible light was negligible. The degradation efficiencies reached 20.0% and 29.8% using PMS alone and PMS/Vis, respectively, which was attributed to the fact that PSM itself was also a strong oxidant and light irradiation promoted the PMS decomposition to generate $\cdot\text{OH}$. It is well known that oxygen vacancies can activate PMS. Therefore, the degradation efficiency over V-doped $\text{Bi}_2\text{MoO}_6/\text{PMS}$ (53.0%) was higher than that over $\text{Bi}_2\text{MoO}_6/\text{PMS}$ (40.0%) due to the fact that V-doped $\text{Bi}_2\text{MoO}_6/\text{PMS}$ possessed more oxygen vacancies, compared with pure Bi_2MoO_6 . Meanwhile, $\text{V}^{5+}/\text{V}^{4+}$ redox cycles might promote PMS activation. The degradation efficiency over V-doped $\text{Bi}_2\text{MoO}_6/\text{Vis}$ (34.1%) was higher than that over $\text{Bi}_2\text{MoO}_6/\text{Vis}$ (25.2%). Pure Bi_2MoO_6 held a relatively low capacity for the separation of photogenerated charges, and V doping could facilitate the separation of photogenerated charges. The degradation efficiency could be reached 95.1% over V-doped $\text{Bi}_2\text{MoO}_6/\text{PMS}/\text{Vis}$ after 20 min reaction. The corresponding TOC removal efficiency reached about 72.8% (Fig. S10). It was worth noting here that the adsorption rate of 30 min dark adsorption was the same as that of 50 min dark adsorption (Fig. S11), indicating that 30 min dark

adsorption had reached adsorption equilibrium and that the decrease in sulfapyridine concentration was mainly due to catalytic degradation rather than adsorption by the catalyst. The preliminary conclusion was that oxygen vacancies, redox cycles, and photocatalysis provided a synergistic effect to activate the PMS, which in turn increased the degradation efficiency. Compared to the few previous reports on the degradation of sulfapyridine, the degradation efficiency and kinetics of V-doped $\text{Bi}_2\text{MoO}_6/\text{PMS}/\text{Vis}$ were superior to those reports (Table S1). In addition, the reuse experiments showed that the degradation efficiency of the recovered samples for sulfapyridine increased by 4.9% relative to the initial degradation efficiency, reaching 100% (Fig. S12), which was attributed to the fact that the oxygen vacancy content of the catalyst increases with the increase of light time (Fig. S13). The concentrations of leached Bi, V, Mo were 0.0627, 0.0328, and 1.4631 $\text{mg}\cdot\text{L}^{-1}$, respectively (Table S2). The leaching of V and Mo provided preliminary evidence that V and Mo were directly involved in the activation of PMS. The leaching of Mo weakened the Bi-O bond while the pH of the reaction solution was 3, resulting in the leaching of a certain amount of Bi ions. However, the Bi and V leaching concentrations was below international emission standards. Compared to other reports [53,54], the leaching concentration of Mo was very low.

In order to verify the environmental resistance of this catalytic system for the degradation of sulfapyridine, the environmental coexisting anion, such as Cl^- , NO_3^- , H_2PO_4^- , HCO_3^- and the environmental coexisting organic matter, humic acid, were separately added to the above catalytic system to observe their effects on the degradation of sulfapyridine. The results indicated that Cl^- , NO_3^- , and H_2PO_4^- had no effect on the degradation efficiency of sulfapyridine, except for HA and HCO_3^- , which had a slight effect on the degradation efficiency of sulfapyridine (Fig. S14). This was because HA affected light penetration in reaction solution [5] and HCO_3^- trapped $\text{SO}_4^{\cdot-}$ and $\cdot\text{OH}$ to produce low activity of HCO_3^{\cdot} and $\text{CO}_3^{\cdot-}$, respectively [13].

To further evaluate the universality of this catalytic system, we used V-doped $\text{Bi}_2\text{MoO}_6/\text{PMS}/\text{Vis}$ catalytic system to degrade three other antibiotics, such as sulfamethoxazole, sulfachloropyridazine, and tetracycline, and the results proved that this catalytic system could still

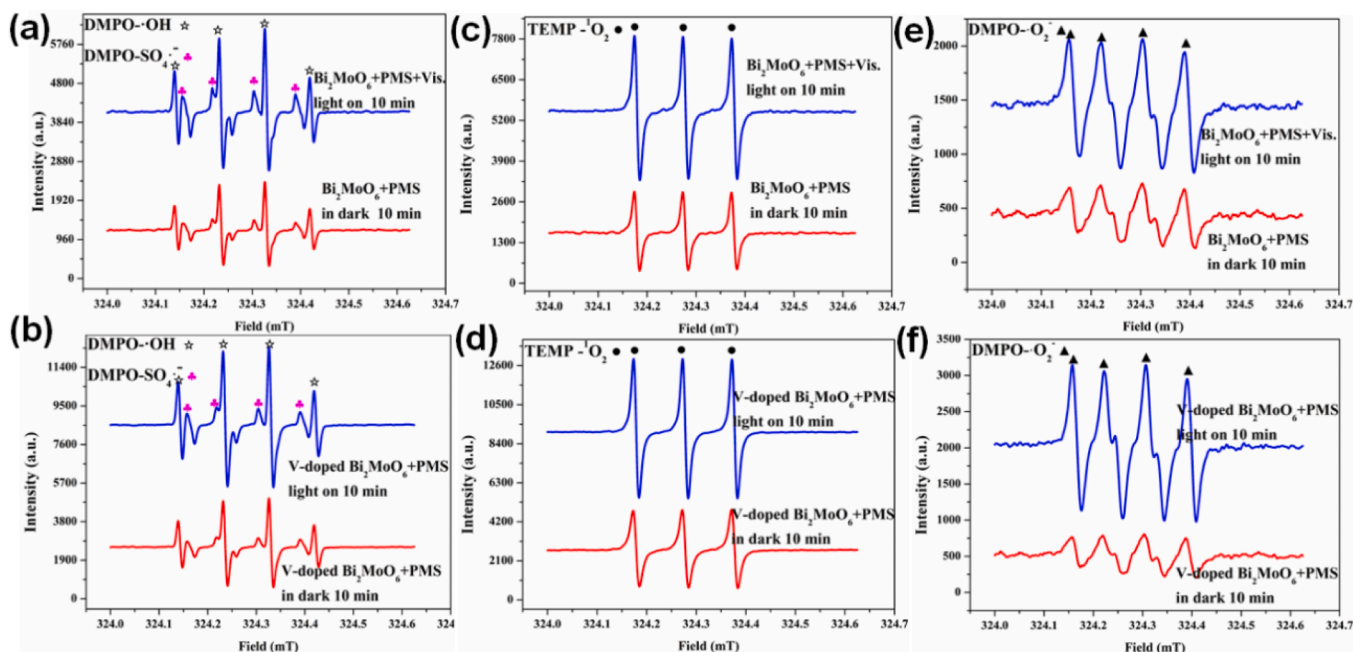


Fig. 5. EPR spectra in the different catalytic systems, (a, b) DMPO for $\text{SO}_4^{\bullet-}$, $\bullet\text{OH}$, (c, d) TEMP for $^1\text{O}_2$, and (e, f) DMPO for $\bullet\text{O}_2^-$.

completely degrade the above three antibiotics under the same conditions (Fig. S15).

3.3. Degradation reaction mechanism

In order to identify the active species that played a dominant role in the degradation of sulfapyridine, a series of quenching experiments of active species were performed. Methanol and tert-butyl alcohol were commonly used to verify the contribution of $\text{SO}_4^{\bullet-}$ and $\bullet\text{OH}$ to

degradation due to the order of magnitude difference in their rate constants [5,13]. In addition, L-Histidine, benzoquinone, EDTD-2Na, and $\text{K}_2\text{Cr}_2\text{O}_7$ were used as capture agents for $^1\text{O}_2$, $\bullet\text{O}_2^-$, h^+ , and e^- [5,14], respectively. As shown in Fig. S16, when a certain amount of methanol and tert-butanol was added to the reaction system, the degradation efficiency decreased from 95.1% to 70.0% and 78%, respectively. This indicated that $\text{SO}_4^{\bullet-}$ and $\bullet\text{OH}$ were generated in V-doped $\text{Bi}_2\text{MoO}_6/\text{PMS}/\text{Vis}$ system and the contribution of $\bullet\text{OH}$ to the sulfapyridine degradation was greater than that of $\text{SO}_4^{\bullet-}$. When L-histidine and

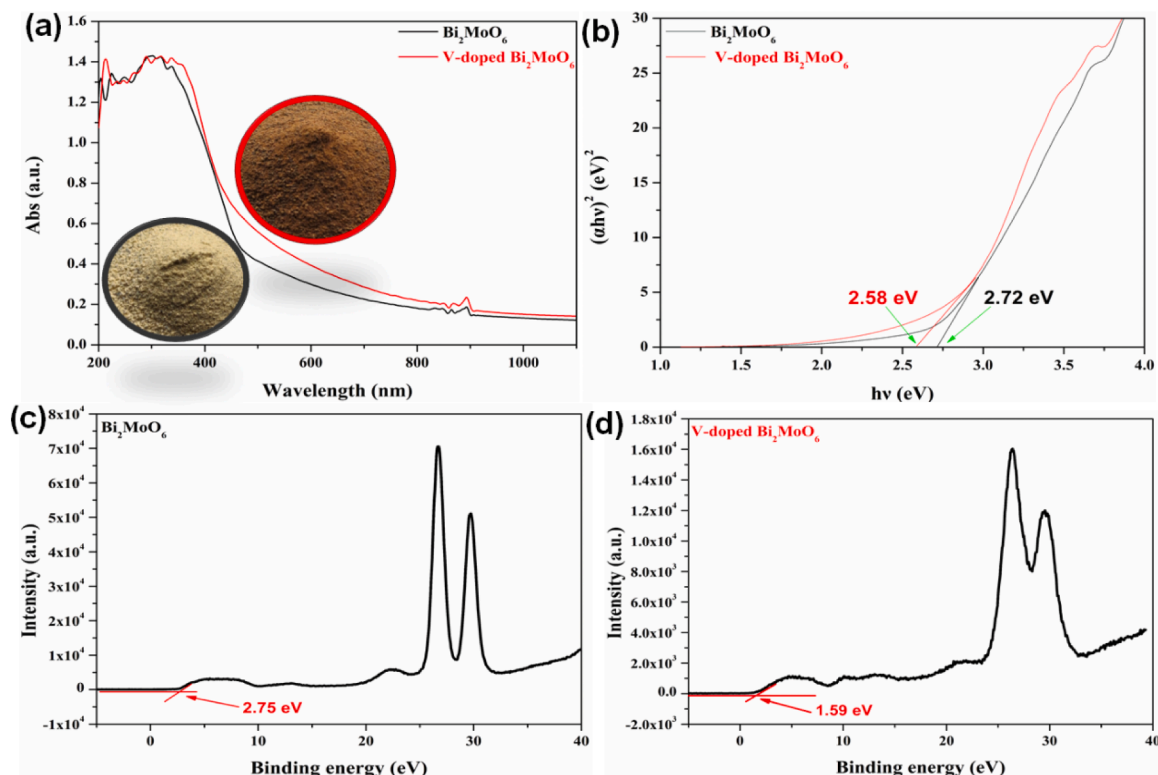


Fig. 6. UV-vis DRS spectra of the as-prepared samples (a) and corresponding bandgap energy (b), valence band spectra (c, d) by XPS tests.

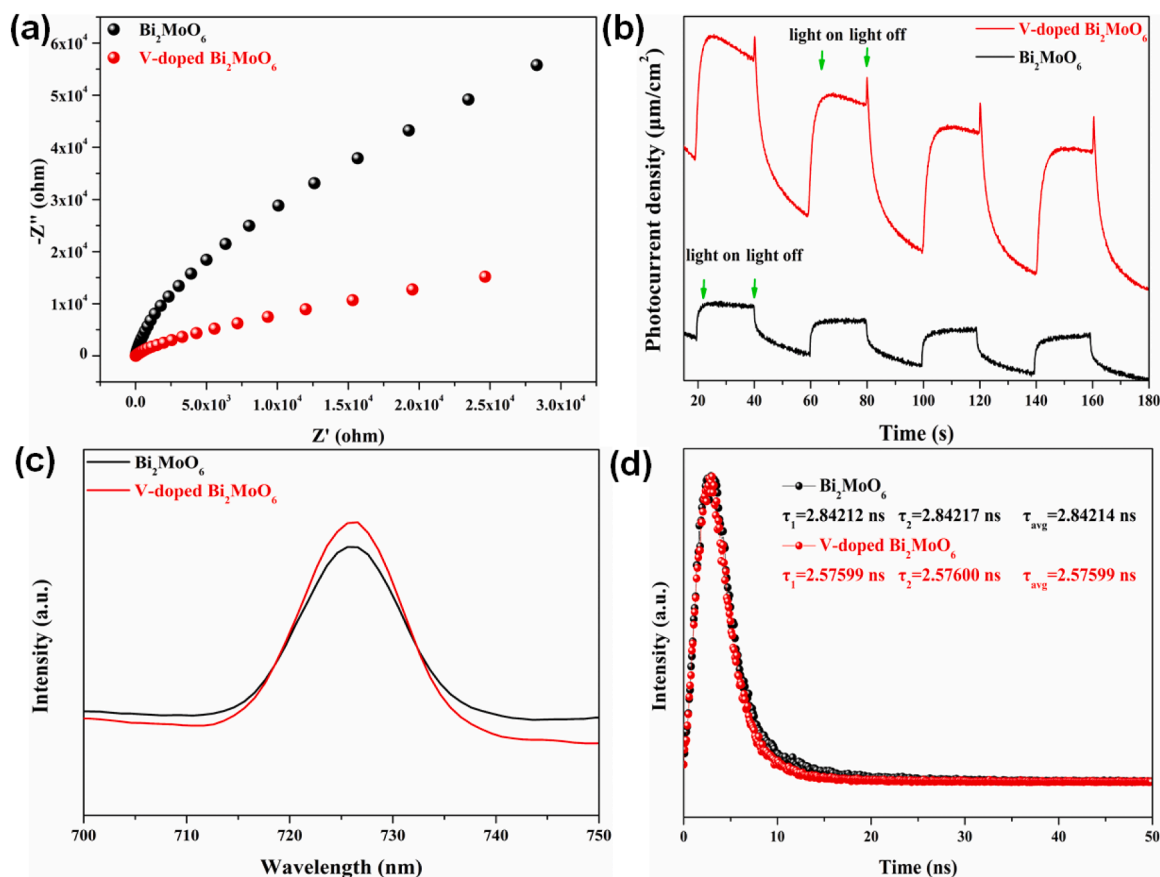


Fig. 7. EIS spectra (a), photocurrent density curves (b), PL spectra (c) and the corresponding Time-resolved photoluminescence (TRPL) spectra (d) of Bi_2MoO_6 and V-doped Bi_2MoO_6 .

benzoquinone were present in the reaction system, the degradation efficiency decreased from 95.1% to 75.0% and 69%, respectively. On the one hand, this suggested the presence of $^1\text{O}_2$ and $^{\bullet}\text{O}_2^-$; on the other hand, it also demonstrated that the contribution of $^{\bullet}\text{O}_2^-$ to the sulfapyridine degradation was more significant than that of $^1\text{O}_2$. However, when $\text{K}_2\text{Cr}_2\text{O}_7$ was added to the reaction system, the degradation efficiency and kinetics were increased. This was because $\text{K}_2\text{Cr}_2\text{O}_7$ trapped the e^- and prolonged the lifetime of the h^+ . The h^+ might play a critical role in the sulfapyridine degradation. When EDTA-2Na was added to the reaction system, the degradation efficiency decreased from 95.1% to 56.0%. This experimental result was consistent with the above conclusion. The h^+ could directly oxidize sulfapyridine, while the h^+ activating PMS should be the main pathway for PMS activation in V-doped $\text{Bi}_2\text{MoO}_6/\text{PMS}/\text{Vis}$ system.

EPR studies were performed to confirm the type of active species and the catalytic mechanism. A 1:2:2:1 peak intensity ratio was attributed to the $\text{DMPO}\cdot^{\bullet}\text{OH}$ signal [9,55] in the four catalytic systems (Fig. 5a, b). The accompanying $\text{DMPO}\cdot\text{SO}_4^{\bullet-}$ signal was clearly observed (Fig. 5a, b). The three peaks with a peak intensity ratio of 1:1:1 over the four catalytic systems (Fig. 5c, d) were assigned to the $\text{TEMP}\cdot^1\text{O}_2$ signal [5,13]. The four peaks with a peak intensity ratio of 1:1:1:1 were identified as the $\text{DMPO}\cdot^{\bullet}\text{O}_2^-$ signal [56,57]. These phenomena verified the presence of $\text{SO}_4^{\bullet-}$, $^{\bullet}\text{OH}$, $^1\text{O}_2$, and $^{\bullet}\text{O}_2^-$.

Both V-doped Bi_2MoO_6 and pure Bi_2MoO_6 activated PMS in the absence of light, and the signal intensity of the active species produced by the PMS activation of by the V-doped Bi_2MoO_6 was greater than that of the pure Bi_2MoO_6 . The square of the signal intensity value of the active species was equal to the corresponding yield [58]. The V doping induced more oxygen vacancies in the Bi_2MoO_6 (Fig. S6). The oxygen vacancies of Bi_2MoO_6 and V-doped Bi_2MoO_6 increased with increasing light exposure time (Fig. S17 a, b), because the photogenerated electrons

reduced the Mo element, lowering the coordination number and losing oxygen, creating more oxygen vacancies. The signal intensity of the oxygen vacancy of the V-doped Bi_2MoO_6 was higher than that of the pure Bi_2MoO_6 . Besides, V^{5+} could enhance the surface reaction and thus activated the PMS through the $\text{V}^{5+}/\text{V}^{4+}$ redox cycle [59,60].

The signal intensity of the active species was stronger in the $\text{Bi}_2\text{MoO}_6/\text{PMS}/\text{Vis}$ (V-doped $\text{Bi}_2\text{MoO}_6/\text{PMS}/\text{Vis}$) than in the $\text{Bi}_2\text{MoO}_6/\text{PMS}$ (V-doped $\text{Bi}_2\text{MoO}_6/\text{PMS}$) at different reaction time (Fig. 5, Fig. S18). This again proved that photocatalytic activation of PMS was the main catalytic reaction pathway.

The V doping enhanced the photocatalysis of Bi_2MoO_6 . Therefore, photocatalytic activation, oxygen vacancy activation and direct activation of the $\text{V}^{5+}/\text{V}^{4+}$ redox cycle produced synergistic effects to enhance the catalytic reaction efficiency of Bi_2MoO_6 .

3.4. The enhancement mechanism of catalytic activity

It was found by many experiments above that V doping enhanced the catalytic activity of Bi_2MoO_6 . Next, experiments and theoretical calculations were combined to investigate the mechanism of enhanced catalytic activity. The Bi_2MoO_6 could absorb light in the ultraviolet, visible, and even near infrared (Fig. 6a). The V-doping strengthened the intensity of light absorption. Apparently, the V-doping changed the color of Bi_2MoO_6 from light yellow to dark brown (Fig. 6a, Inset). Essentially, the V-doping narrowed the band gap width of Bi_2MoO_6 and changed its energy band structure. The values of the band gap were calculated on the basis of $ah\nu^n = A(h\nu - E_g)$, where A , E_g , α , and $h\nu$ are the absorbance, band gap, absorption coefficient, and incident photon energy of the corresponding semiconductor, respectively. The band gap (E_g) values of Bi_2MoO_6 and V-doped Bi_2MoO_6 were 2.72 eV [43,61] and 2.58 eV, respectively (Fig. 6b). The valence band positions (E_{VB}) of

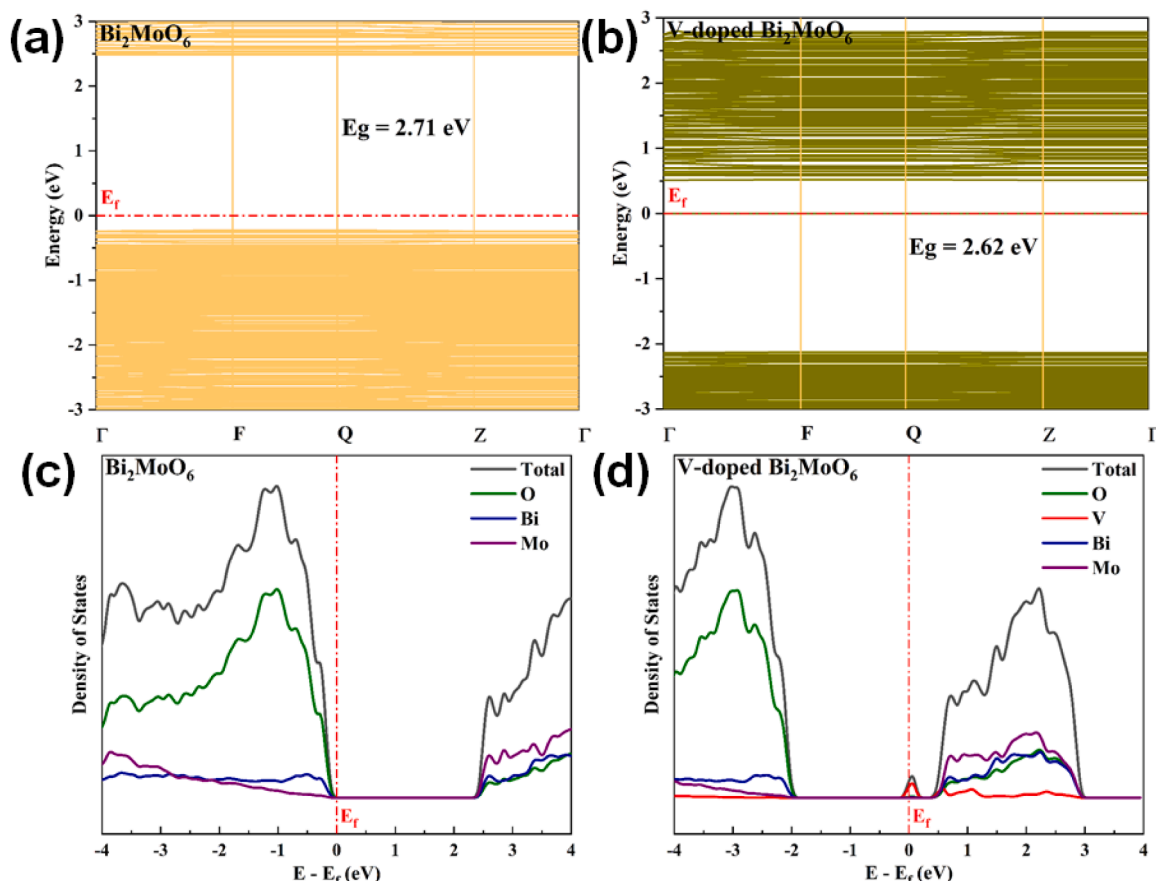


Fig. 8. The band structures of Bi_2MoO_6 (a) and V-doped Bi_2MoO_6 (b), and their corresponding density of states (DOS) plots (c, and d).

Bi_2MoO_6 and V-doped Bi_2MoO_6 were determined by XPS at 2.75 eV and 1.59 eV, respectively (Fig. 6c,d). Thus, the conduction band positions (E_{CB}) of the two samples were obtained by E_{VB} subtracting E_{g} , which were 0.03 eV and -0.99 eV, respectively, as shown in the schematic diagram of energy band structure (Fig. S19). Therefore, V doping enabled Bi_2MoO_6 to greatly amplify the reduction of photogenerated electrons while maintaining sufficient oxidation of photogenerated holes. Meanwhile, optical corrosion of Bi_2MoO_6 was mitigated by the slight reduction in the oxidation capacity of photogenerated holes.

Electrochemical and photoelectrochemical tests were performed to study the migration and separation of photogenerated charges. Electrochemical impedance spectroscopy (EIS) demonstrated that the radius of the impedance curve of the V-doped Bi_2MoO_6 sample was smaller than that of the pure Bi_2MoO_6 (Fig. 7a), indicating that photogenerated charge migration was more easily accomplished in the V-doped Bi_2MoO_6 sample than in the pure Bi_2MoO_6 . The photocurrent density of the V-doped Bi_2MoO_6 was stronger in comparison to the pure Bi_2MoO_6 (Fig. 7b), which suggested a more efficient separation of photogenerated charges in the V-doped Bi_2MoO_6 . An anomaly was the fact that the PL intensity of the V-doped Bi_2MoO_6 was brighter than that of the pure Bi_2MoO_6 (Fig. 7c), indicating the presence of non-radiative transition of photogenerated electrons and impurity energy levels induced by V-doping in the V-doped Bi_2MoO_6 (Fig. S20) [56,62]. The average lifetimes of the photogenerated electrons for the V-doped Bi_2MoO_6 and pure Bi_2MoO_6 tested by TRPL were 2.57599 ns and 2.84214 ns, respectively (Fig. 7d). This result was a further confirmation of the above conclusion that the impurity energy levels caused the non-radiative jump of the photogenerated electrons, which in turn led to the shortening of the lifetime.

To verify the above experimental conclusions, we calculated the energy band structures and density of states. The calculated self-

consistent band structures of pure Bi_2MoO_6 and V-doped Bi_2MoO_6 are shown in Fig. 8. The band gap values were 2.71 eV and 2.62 eV for pristine Bi_2MoO_6 and V-doped Bi_2MoO_6 , respectively, which were in general agreement with the optical band gap (2.72 eV for pristine Bi_2MoO_6 and 2.58 eV V-doped Bi_2MoO_6) estimated from the UV-Vis DRS (Fig. 6b). It was also confirmed that V-doping could narrow the band gap of Bi_2MoO_6 . The more energy bands were found in the band diagram of the V dopant due to the lower symmetry and greater distortion in the structure of V-doped Bi_2MoO_6 . As shown in Fig. 8b, new states appeared in the band gap around the Fermi level, leading to the formation of impurity energy level.

The density of states (DOS) for Bi, O, Mo, and V atoms are shown in Fig. 8c,d. The lower conduction band of Bi_2MoO_6 was mainly composed of the states of Mo, and the contributions of Bi and O states were smaller. The upper valence band consisted mainly of O states. Therefore, interactions between Mo and O atoms could have a significant influence on the band structure of Bi_2MoO_6 . With the introduction of V, the composition of the valence band of Bi_2MoO_6 in Fig. 8d did not change. However, V doping had induced a new energy level in Bi_2MoO_6 at the Fermi level, which consisted mainly of V state. Meanwhile, the interaction of V-Mo formed the impurity energy level (subband) mainly composed of V state at conduction band edge. The results were consistent with the judgment of the PL and TRPL analyses. Moreover, the conduction band of V-doped Bi_2MoO_6 was mainly composed of Bi, Mo, V, and O states, whose orbital overlap was strong, indicating a stronger interaction with each other and favoring the formation of stable Bi(Mo)-O-V bonds with high covalency. The covalent nature of these metal-oxygen bridge bonds facilitated the transfer of electrons from Bi(Mo) atoms to V, which in turn accelerated the $\text{V}^{5+}/\text{V}^{4+}$ redox cycle, further enhancing the surface reaction.

The adsorption configurations of the PMS on catalyst, water

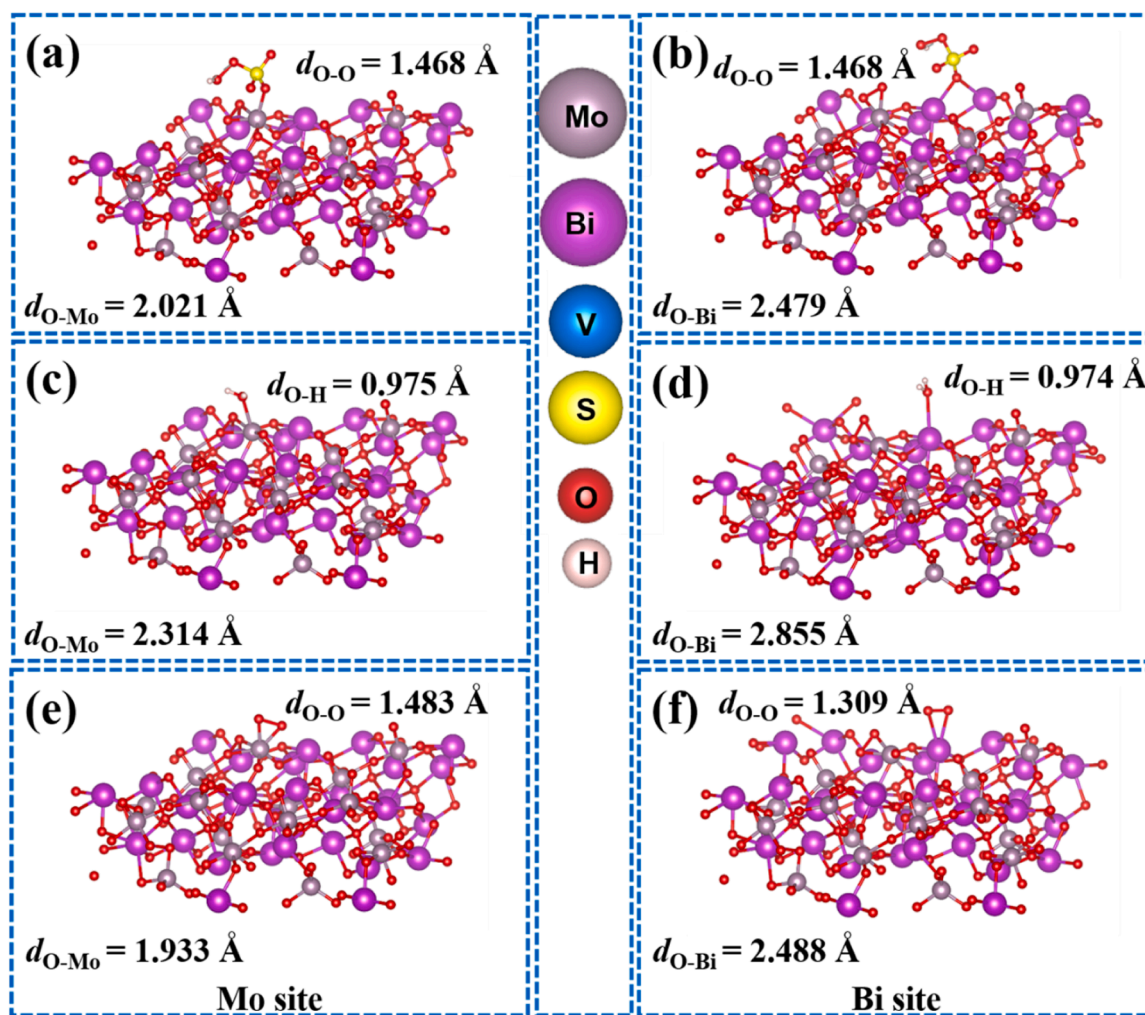


Fig. 9. Optimized configurations of PMS, H₂O and O₂ adsorbed on Bi₂MoO₆, Mo site (a, c, e), and Bi site (b, d, f) on pure Bi₂MoO₆.

molecule and dissolved oxygen (Fig. 9 and Fig. 10) were constructed by DFT calculations, and the effects of V-doping on the main active sites were determined by considering the chemical bonds and adsorption energies.

Fig. 9a and b demonstrate that the O-O bond length of PMS ($d_{O-O} = 1.468$ Å) at the Bi site is similar to that at the Mo site. However, the Mo-O bond length ($d_{Mo-O} = 2.021$ Å) for PMS adsorption at the Mo site is shorter than the Bi-O bond length ($d_{Bi-O} = 2.479$ Å) for PMS adsorption at the Bi site. The O-O bond length of PMS ($d_{O-O} = 1.468$ Å) at the V site was found to be longer than that of free PMS ($d_{O-O} = 1.326$ Å) [13]. This longer bond length makes the O-O bond more susceptible to cleavage by electrons from V^{5+}/V^{4+} redox cycles and photogenerated electrons on the V impurity energy level, which are transferred through the V-O bond. When PMS was adsorbed on the Mo and Bi sites of V-doped Bi₂MoO₆, the O-O bonds of PMS had similar bond lengths ($d_{O-O} = 1.469$ Å on Mo and $d_{O-O} = 1.471$ Å on Bi). However, the corresponding Mo-O bond length ($d_{Mo-O} = 1.977$ Å) was still shorter than the Bi-O bond length ($d_{Bi-O} = 2.699$ Å). Furthermore, the adsorption energy of PMS on the V site (-4.29 eV) was smaller than that on the Mo (1.32 eV) and Bi (-4.41 eV) sites, indicating that the Bi site remained the main active site for photocatalytic activation of PMS. This observation is consistent with the fact that the addition of V atom and O vacancy did not alter the composition of the valence band (Fig. 8d). Additionally, the adsorption energy of PMS at the Bi site on V-doped Bi₂MoO₆ (-4.41 eV) was smaller than that of PMS at the Mo site on pure Bi₂MoO₆ (1.28 eV) (Fig. S21). Therefore, PMS adsorbed on Bi sites of V-doped Bi₂MoO₆ exhibited a

higher tendency for activation compared to PMS adsorbed on Mo sites of pure Bi₂MoO₆.

In Fig. 9c and d, it can be observed that when H₂O was adsorbed on the Mo and Bi sites in pure Bi₂MoO₆, the Mo-O and Bi-O bond lengths were measured to be 2.314 Å and 2.855 Å, respectively. The adsorption energies of H₂O at the Mo and Bi sites in pure Bi₂MoO₆ were found to be 2.55 eV and 2.78 eV, respectively (Fig. S22). These findings indicate that the interaction between H₂O and the Mo site was stronger compared to the interaction with the Bi site. Additionally, the adsorption energy of H₂O at the Mo site in V-doped Bi₂MoO₆ (-0.19 eV) was lower than that of H₂O at the Mo site in Bi₂MoO₆ (2.55 eV). Furthermore, the adsorption energies of H₂O at the Bi (-0.41 eV) and V (-0.85 eV) sites in V-doped Bi₂MoO₆ were even lower than at the Mo site. This suggests that V doping with O vacancy altered the electronic structure of Bi₂MoO₆ (Fig. S23 and Fig. S24), with the V site becoming the primary active site for the adsorption of activated water, exhibiting a strong interaction with H₂O ($d_{V-O} = 2.101$ Å $<$ $d_{Mo-O} = 2.543$ Å $<$ $d_{Bi-O} = 2.898$ Å) (Fig. 10d, e, f).

The optimized configuration for the adsorption of dissolved oxygen on the Bi₂MoO₆ surface is depicted in Fig. 9e, f. This configuration demonstrates a reciprocal relationship between metal-oxygen and oxygen-oxygen bonds, indicating the stability of these adsorption configurations. The adsorption energies for O₂ on the Mo and Bi sites in Bi₂MoO₆ were 0.69 eV and -0.07 eV, respectively. This suggests that the activation of O₂ by Bi sites is slightly stronger than that by Mo sites. The introduction of V atom and O vacancy resulted in the formation of

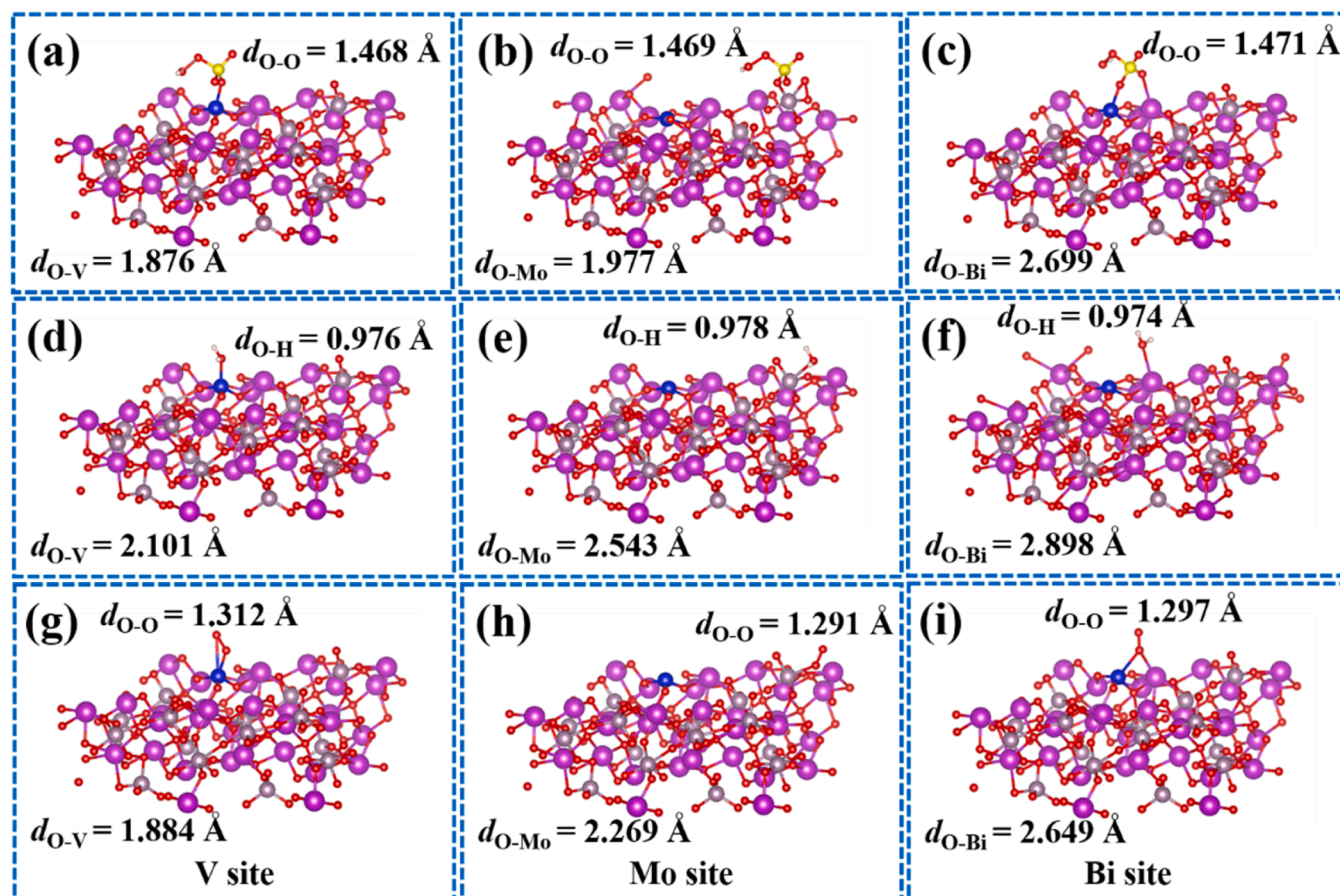


Fig. 10. Optimized configurations of PMS, H₂O and O₂ adsorbed on V-doped Bi₂MoO₆, V site (a, d, g), Mo site (b, e, h), and Bi site (c, f, i) on V-doped Bi₂MoO₆.

metal-oxygen bridge bonds Bi(Mo)-O-V, especially the formation of Bi-O-Mo-O-V, which altered the charge distribution due to the differing electronegativities of these atoms. V-doped Bi₂MoO₆ exhibited a higher concentration of electrons from the V atom surrounding the Mo atom, as depicted in Fig. S23 and S24. Consequently, the interaction between the Mo site and O₂ was enhanced, leading to a decrease in the corresponding adsorption energy from 0.69 to −0.40 eV. Moreover, the adsorption energy of O₂ at the V site (−2.70 eV) was smaller compared to both the Mo site (−0.40 eV) and Bi site (−1.32 eV), as shown in Fig. S25. This indicates that the V site in V-doped Bi₂MoO₆ was the primary active site for O₂ activation.

The Mo 3d_{5/2} binding energy increased from 232.10 eV before to 232.30 eV after the reaction, and the V 2p_{3/2} binding energy increased from 515.77 eV before to 516.93 eV after the reaction (Fig. S26), indicating that Mo⁵⁺/V⁴⁺ participated in the PMS activation [63]. The binding energy was dependent on the surrounding chemical environment [64]. After the reaction, the binding energy of Bi 4f_{7/2} also increased by 0.38 eV (Fig. S26), which could be due to the leaching of Bi ions or Mo ions [64].

Based on the above results, the catalytic reaction mechanism could be proposed. Under visible light irradiation, the valence band electrons in the O 2s, Mo 4p, Bi 6s, and V 4s orbitals transferred to the Mo 4d and 5s orbitals, Bi 6p orbitals, V 3d, and O 2p orbitals in the conduction band, leaving holes in the valence band (Eq. 5). Then the photogenerated electrons possessing higher energy, jumped to the V 3d orbitals at the doped energy level by non-radiative transition, stayed for a moment, and then returned to the valence band by radiative transition. It was the dwelling time of the photogenerated electrons that prolongs the lifetime of the photogenerated holes in the valence band. In this way, photogenerated electrons could activate dissolved oxygen and PMS to

produce [•]O₂[−] and SO₄^{•−}, respectively (Eqs. 6, 7). Under the same conditions, when PMS was added to the catalytic system, less [•]O₂[−] was produced (Fig. S27), indicating the presence of a competitive effect between PMS and dissolved oxygen for obtaining photogenerated e[−], on the other hand, the main source of [•]O₂[−] was the reduction reaction of photogenerated e[−] to adsorbed oxygen. Meanwhile, the competition between PMS and dissolved oxygen for access to photogenerated e[−] promoted the separation of photogenerated charges and prolonged the lifetime of photogenerated h⁺. The redox potential of [•]OH/H₂O was 2.38 eV, the photogenerated h⁺ (E = 1.59 eV) could not activate water molecules to produce [•]OH and could only activate PMS to generate SO₅^{•−} (Eq. 8). The standard redox potentials of V⁵⁺/V⁴⁺, HSO₅[−]/SO₅^{•−}, and HSO₅[−]/SO₄^{•−} were 1.0, 1.1, and 2.6–3.1 eV [5,13,65], respectively. The potential of photoinduced electrons in V-doped Bi₂MoO₆ system was −0.99 eV. On the one hand, V⁵⁺ could be reduced to V⁴⁺ by photogenerated e[−] (Eq. 9); on the other hand, the V⁵⁺/V⁴⁺ redox cycle could directly activate PMS to produce SO₄^{•−} and SO₅^{•−} (Eqs. 10, 11). Like the V⁵⁺/V⁴⁺ redox cycle, the Mo⁵⁺/Mo⁶⁺ redox cycle could also activate PMS [63,66] and the Mo⁶⁺ could be reduced to Mo⁵⁺ by photogenerated e[−] (Eqs. 12–14). Besides, oxygen vacancies could also activate PMS to form SO₄^{•−} and [•]O₂[−] by electron transfer (Eqs. 15, 16). The ¹O₂ could be derived from SO₅^{•−} or [•]O₂[−] (Eqs. 17–19). By comparing the production of ¹O₂ in three cases: pure photocatalysis, photocatalytic activation of PMS, and photocatalytic activation of PMS in oxygen-free water solution (Fig. S28), it was found that the introduction of PMS increased the yield of ¹O₂. And the highest amount of ¹O₂ was produced in the case of photocatalytic activation of PMS in oxygen-free aqueous solution, which indicated that the ¹O₂ mainly stemmed from the PMS activation. Finally, the generated active species, including SO₄^{•−}, [•]OH, ¹O₂, [•]O₂[−], h⁺ and e[−] would decompose the sulfapyridine molecules to CO₂ and H₂O.

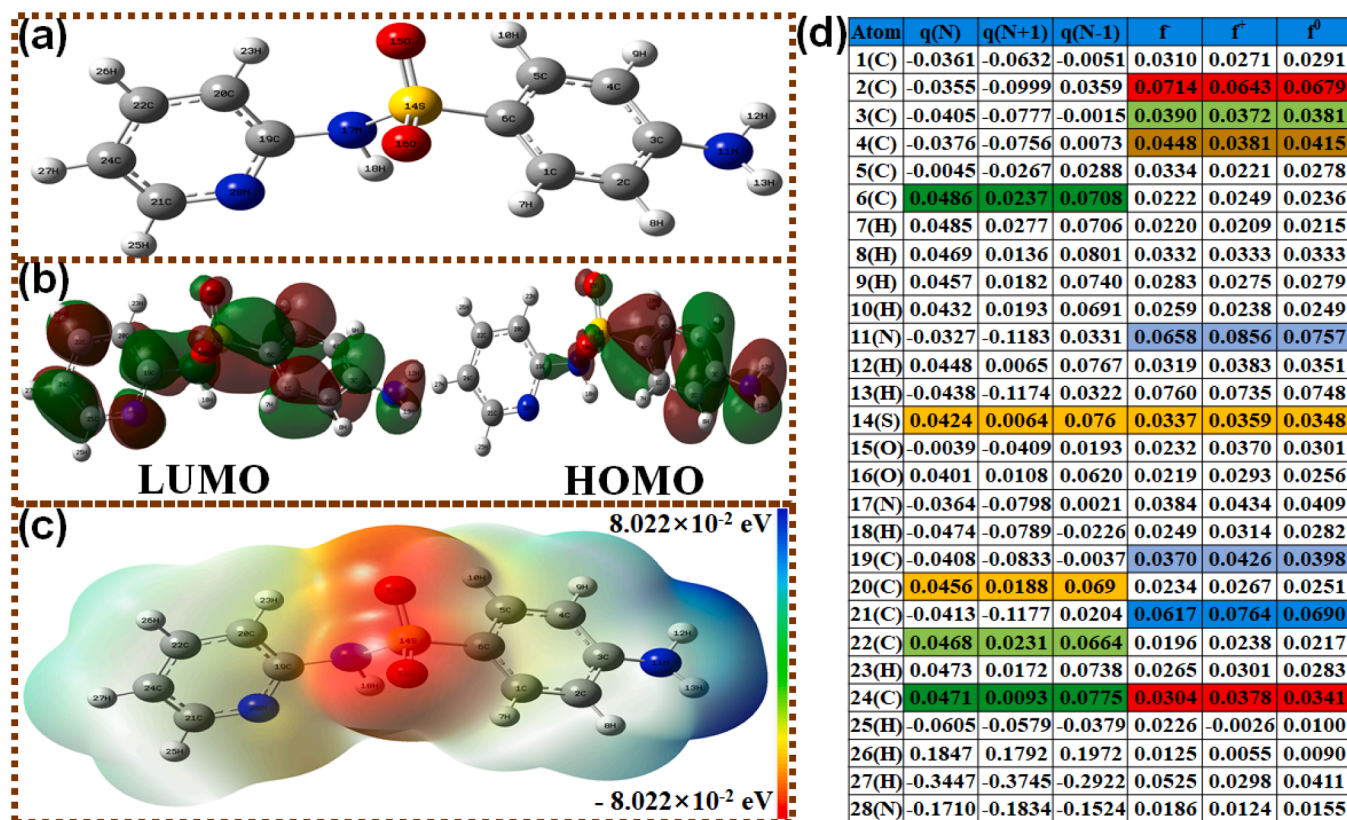
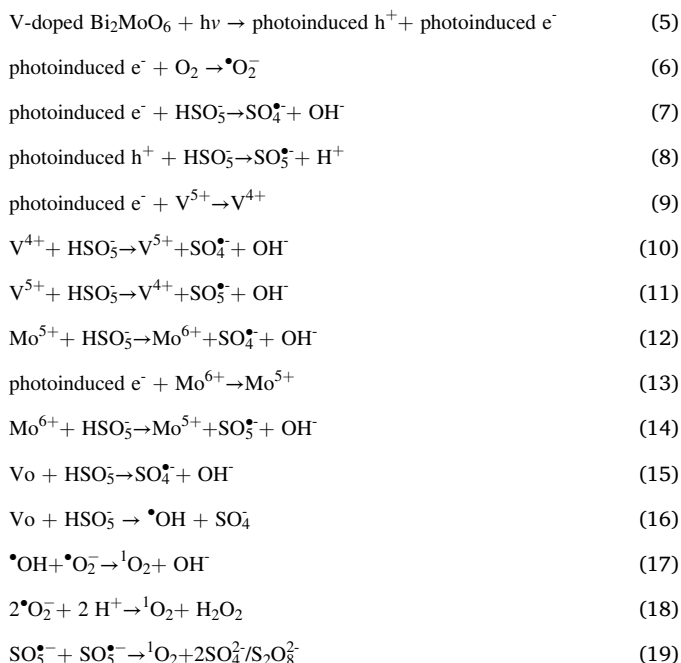


Fig. 11. DFT calculations on sulfapyridine molecule: sulfapyridine molecule structure (a), the lowest unoccupied molecular orbital (LUMO) and the highest occupied molecular orbital (HOMO)(b), electrostatic potential (ESP)-mapped molecular surface of sulfapyridine (c), natural population analysis (NPA) charge distribution and Fukui index of sulfapyridine (d).



3.5. Degradation pathway and toxicity assessment of intermediate products

The intermediates of sulfapyridine were investigated by means of LC-

MS. In order to obtain reliable intermediates and reaction pathways, DFT calculation was used to clarify the sulfapyridine molecule and the sites in the sulfapyridine molecule susceptible to attack by reactive oxygen species. The charge distribution including molecular orbital, electrostatic potential and Fukui index of sulfapyridine were calculated. The corresponding profiles and Fukui index are shown in Fig. 11. The HOMO denotes the ability to donate electrons, while the LUMO represents the ability to receive electrons [37,67]. Except for 7 H, 8 H, 18 H, 23 H, and 25–27 H, the entire sulfapyridine molecule was susceptible to electrons (Fig. 11b). The sulfapyridine HOMO was distributed in and around atoms 1 through 17, mainly due to thionyl and amino groups. 2 C, 3 C, 4 C, 53 C, 11 N, 14 S, and 17 N in the aromatic ring possessed high f^+ and f^0 (Fig. 11d), showing that these atoms were sensitive to attack by electrophilic oxygen species. Besides, 21 C and 24 C also possessed high f^+ and f^0 (Fig. 11d), indicating that the two C sites were more active.

Along with the dominant roles of h^+ , $\bullet\text{O}_2^-$ and $\bullet\text{OH}$ and mass spectrometry analysis (Fig. S29), the possible degradation pathways of sulfapyridine over the V-doped Bi_2MoO_6 /PMS/Vis system were proposed through the analysis of the chemical structure of sulfapyridine and the corresponding intermediates. As shown in Fig. S30, the pro-position C of the amino group was attacked by the OH group and the degradation pathway I was opened. The N-C chemical bond was cleaved due to the strong electron donating ability of 17 N, further generating P2 and P3 intermediates. Similarly, 14 S was highly reactive. The S-C bond was broken, resulting in the formation of P4. The degradation pathway II was also centered around the highly reactive 14 S, i.e., corresponding to the cleavage of the S-C and S-N bonds. These results were fully consistent with the analyses of the HOMO and Fukui Index.

Although the oral rat LD50 values increased, the toxicity of the product decreased as the reaction time was increased and the aromatic

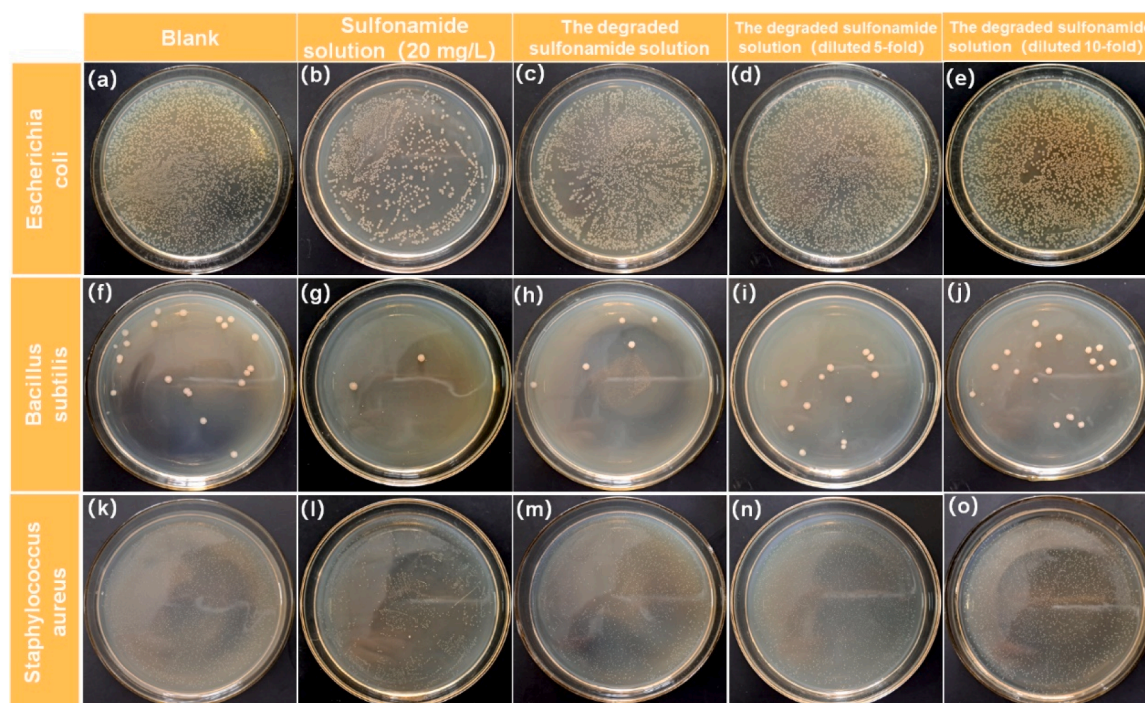


Fig. 12. The inhibition effect over (a, f, k) the blank experiment, (b, g, l) sulfapyridine solution, (c, h, m) the degraded sulfapyridine solution, (d, i, n) the degraded sulfapyridine solution (diluted 5-fold) and (e, j, o) the degraded sulfapyridine solution (diluted 10-fold) for *Escherichia coli*, *Bacillus subtilis*, and *Staphylococcus aureus*, respectively.

ring was further cleaved. The developmental toxicity values decreased, the mutagenicity values were all negative, while P3 and P7 were still “NON-Toxicant”, and the LC50–96hr values increased [37,67] (Table S3), all of which together indicated that sulfapyridine became less toxic through degradation by the V-doped Bi_2MoO_6 /PMS/Vis catalytic system.

To further verify the reduced toxicity of sulfapyridine after degradation, we used sulfapyridine and the degraded sulfapyridine solution to inhibit the growth of *Escherichia coli*, *Bacillus subtilis*, and *Staphylococcus aureus* bacterial strains. From the phenotypes (Fig. 12) and statistics (Fig. S31–S33), it was found that the sulfapyridine solution was able to inhibit three strains of bacteria compared to the blank control, but the degraded sulfapyridine solution showed significantly lower inhibition of the strains, especially the diluted solution which had almost no inhibitory effect on the strains. This further indicated that the sulfapyridine solution was degraded into non-toxic small molecules, which in turn reduced toxicity.

4. Conclusion and outlooks

In this work, V-doped Bi_2MoO_6 was prepared by a simple chemical method. Firstly, the V doping changes the energy band structure of Bi_2MoO_6 , allowing Bi_2MoO_6 to greatly enhance the reduction of photogenerated electrons while maintaining sufficient oxidation of photogenerated holes. Meanwhile, the V doping promoted the formation of impurity energy levels, which contributed to the non-radiative transition of photogenerated electrons, improved the separation efficiency of photogenerated charges, and extended the lifetime of photogenerated holes. Secondly, the V doping introduced the V active site. Further, the V doping improved the adsorption energy of PMS, H_2O and dissolved oxygen on the catalyst surface, making them more readily activated to form active species. Finally, the V doping increased the oxygen vacancy content of Bi_2MoO_6 . Thus, the enhanced photocatalysis, the $\text{V}^{5+}/\text{V}^{4+}$ redox cycle, and the increased oxygen vacancies due to V doping produced a synergistic catalytic activation of PMS. The dominant h^+ , $\bullet\text{O}_2^-$ and $\bullet\text{OH}$ could completely degrade sulfapyridine after 20 min reaction

in V- Bi_2MoO_6 /PMS/Vis catalytic system. This highly stable catalytic system is expected to be used for the treatment of other organic wastewaters.

CRediT authorship contribution statement

Jun Yang: Investigation, Funding acquisition, Writing - original draft. **Taiping Xie:** Supervision, Resources, Funding acquisition, Writing - review & editing. **Yuhan Mei:** Investigation, Writing - original draft. **Junyu Chen:** Investigation, Software, Methodology, Validation. **Hao Sun:** Investigation, Software, Methodology, Validation. **Shan Feng:** Investigation, Software, Methodology, Validation. **Yu Zhang:** Investigation, Software, Methodology, Validation. **Ying Zhao:** Investigation, Software, Methodology, Validation. **Jiankang Wang:** Validation, Resources, Supervision, Writing - review & editing. **Xiaoqing Li:** Validation, Funding acquisition. **Jiahong He:** Data curation, Validation. **Houyang Chen:** Supervision, Resources, Writing - review & editing.

Declaration of Competing Interest

The authors declare that they have no known competing financial interests or personal relationships that could have appeared to influence the work reported in this paper.

Data Availability

Data will be made available on request.

Acknowledgements

This work was supported by the Spires project of Chongqing University of Arts and Sciences (P2020HH07), Chongqing Basic Science Advanced Technology Research Program (CSTB2022NSCQ-MSX1397 and 2022NSCQ-MSX0780), Science and Technology Research Program of Chongqing Municipal Education Commission (KJZD-M202301301, KJQN202204508), Science and Technology Fund Project of Guizhou

Province (No.[2018]1415).

Appendix A. Supporting information

Supplementary data associated with this article can be found in the online version at doi:10.1016/j.apcatb.2023.123149.

References

- [1] Y. He, J. Qian, P. Wang, T. Xie, D.D. Dionysiou, B. Lu, S. Tang, Synergized selenium-vacancy heterogeneous interface and carbon nanotubes for insight into efficient oxidation of pollutants via photocatalytic peroxymonosulfate activation, *Appl. Catal. B: Environ.* 330 (2023), 122620.
- [2] D. Yu, J. He, T. Xie, Q. Xu, G. Li, L. Du, J. Huang, J. Yang, W. Li, J. Wang, Peroxymonosulfate activation using a composite of copper and nickel oxide coated on SBA-15 for the removal of sulfonamide antibiotics, *Environ. Res.* (2021), 112301.
- [3] H. Liu, B. Zhang, Y. Li, Q. Fang, Z. Hou, S. Tian, J. Gu, Effect of radical species and operating parameters on the degradation of sulfapyridine using a UV/chlorine system, *Ind. Eng. Chem. Res.* 59 (2020) 1505–1516.
- [4] J. Ji, C. Shi, L. Xu, K. Zhang, Y. Zhang, C. Li, E. Lichtfouse, Degradation of sulfapyridine antibiotics by chlorination in a pilot-scale water distribution system: kinetics, THMs, and DFT studies, *Environ. Sci.: Water Res. Technol.* 8 (2022) 2207–2215.
- [5] S. Feng, M. Yu, T. Xie, T. Li, D. Kong, J. Yang, C. Cheng, H. Chen, J. Wang, $\text{MoS}_2/\text{CoFe}_2\text{O}_4$ heterojunction for boosting photogenerated carrier separation and the dominant role in enhancing peroxymonosulfate activation, *Chem. Eng. J.* 433 (2022), 134467.
- [6] P. Cheng, Y. Wang, M. Sarakha, G. Mailhot, Enhancement of the photocatalytic activity of decatungstate, $\text{W}_{10}\text{O}_{32}$, for the oxidation of sulfasalazine/sulfapyridine in the presence of hydrogen peroxide, *J. Photochem. Photobiol. A: Chem.* 404 (2021).
- [7] K. Li, M. Chen, L. Chen, S. Zhao, W. Xue, Z. Han, Y. Han, F. Zhang, Y. Yan, Y. Dong, In-situ hydrothermal synthesis of $\text{Ag}_3\text{PO}_4/\text{g-C}_3\text{N}_4$ nanocomposites and their photocatalytic decomposition of sulfapyridine under visible light, *Processes* 11 (2023).
- [8] S.Y. Zhao, C.X. Chen, J. Ding, S.S. Yang, Y.N. Zang, X.D. Qin, X.L. Gao, Z. Song, N. Q. Ren, Fabrication of AQ2S/GR composite photosensitizer for the simulated solar light-driven degradation of sulfapyridine, *Environ. Sci. Ecotechnol.* 8 (2021), 100111.
- [9] J. He, T. Xie, T. Luo, Q. Xu, F. Ye, J. An, J. Yang, J. Wang, Enhanced peroxymonosulfate activation over heterogeneous catalyst $\text{Cu}_{0.76}\text{Co}_{2.24}\text{O}_4/\text{SBA-15}$ for efficient degradation of sulfapyridine antibiotic, *Ecotoxicol. Environ. Saf.* 216 (2021), 112189.
- [10] D. Yu, J. He, T. Xie, Q. Xu, G. Li, L. Du, J. Huang, J. Yang, W. Li, J. Wang, Peroxymonosulfate activation using a composite of copper and nickel oxide coated on SBA-15 for the removal of sulfonamide antibiotics, *Environ. Res.* 206 (2022), 112301.
- [11] M. Kohantorabi, G. Moussavi, S. Giannakis, A review of the innovations in metal- and carbon-based catalysts explored for heterogeneous peroxymonosulfate (PMS) activation, with focus on radical vs. non-radical degradation pathways of organic contaminants, *Chem. Eng. J.* 411 (2021), 127957.
- [12] S. Giannakis, K.-Y.A. Lin, F. Ghanbari, A review of the recent advances on the treatment of industrial wastewaters by sulfate radical-based advanced oxidation processes (SR-AOPs), *Chem. Eng. J.* 406 (2021), 127083.
- [13] D. Yu, J. He, T. Xie, J. Yang, J. Wang, J. Xie, H. Shi, Z. Gao, B. Xiang, D. D. Dionysiou, Boosting catalytic activity of $\text{SrCoO}_{2.52}$ perovskite by Mn atom implantation for advanced peroxymonosulfate activation, *J. Hazard. Mater.* 442 (2023), 130085.
- [14] D. Yu, J. He, T. Xie, Q. Xu, Q. Zhu, J. Yang, J. An, F. Ye, J. Wang, B. Xiang, New insights into Sr-O bonds enhances Co/Fe catalytic activity in SrCoFe perovskite for boosted peroxymonosulfate activation, *Chem. Eng. J.* 426 (2021), 131525.
- [15] Z. Xu, Y. Wu, X. Wang, Q. Ji, T. Li, H. He, H. Song, S. Yang, S. Li, S. Yan, L. Zhang, Z. Zou, Identifying the role of oxygen vacancy on cobalt-based perovskites towards peroxymonosulfate activation for efficient iohexol degradation, *Appl. Catal. B: Environ.* 319 (2022), 121901.
- [16] C. Hu, N. Tian, Y. Zhang, H. Huang, Facet-selective charge separation in two-dimensional bismuth-based photocatalysts, *Catal. Sci. Technol.* 11 (2021) 3659–3675.
- [17] S. Song, Z. Xing, H. Zhao, Z. Li, Z. Wei, Recent Advances in Bismuth-Based Photocatalysts: Environment and Energy Applications, *Green Energy & Environment*, 2022.
- [18] Q. Meng, C. Lv, J. Sun, W. Hong, W. Xing, L. Qiang, G. Chen, X. Jin, High-efficiency Fe-Mediated Bi_2MoO_6 nitrogen-fixing photocatalyst: reduced surface work function and ameliorated surface reaction, *Appl. Catal. B: Environ.* 256 (2019), 117781.
- [19] S.K. Pradhan, K. Das, R. Bariki, D. Majhi, N. Behera, B.G. Mishra, Facile low temperature reflux synthesis of Bi self-doped Bi_2MoO_6 and construction of $\text{CaFe}_2\text{O}_4/\text{Bi}_2\text{MoO}_6$ 0D QD-2D p-n heterojunction photocatalyst for efficient bisphenol A degradation and Cr(VI) reduction, *Appl. Surf. Sci.* 611 (2023), 155607.
- [20] M. Chakraborty, S. Ghosh, V. Mahalingam, Fe and W doped Bi_2MoO_6 nanoflakes: a promising material for efficient solar water splitting, *Sustain. Energy Fuels* 4 (2020) 1507–1514.
- [21] T. Ma, C. Yang, L. Guo, R.A. Soomro, D. Wang, B. Xu, F. Fu, Refining electronic properties of Bi_2MoO_6 by In-doping for boosting overall nitrogen fixation via relay catalysis, *Appl. Catal. B: Environ.* 330 (2023), 122643.
- [22] J. Wang, C. Zhao, S. Yuan, X. Li, J. Zhang, X. Hu, H. Lin, Y. Wu, Y. He, One-step fabrication of Cu-doped Bi_2MoO_6 microflower for enhancing performance in photocatalytic nitrogen fixation, *J. Colloid Interface Sci.* 638 (2023) 427–438.
- [23] H. Li, W. Li, F. Wang, X. Liu, C. Ren, Fabrication of two lanthanides co-doped Bi_2MoO_6 photocatalyst: selection, design and mechanism of Ln1/Ln2 redox couple for enhancing photocatalytic activity, *Appl. Catal. B: Environ.* 217 (2017) 378–387.
- [24] D.P. Dutta, A. Ballal, S. Chopade, A. Kumar, A study on the effect of transition metal (Ti^{4+} , Mn^{2+} , Cu^{2+} and Zn^{2+})-doping on visible light photocatalytic activity of Bi_2MoO_6 nanorods, *J. Photochem. Photobiol. A: Chem.* 346 (2017) 105–112.
- [25] Q. Zhou, N. Li, D. Chen, Q. Xu, H. Li, J. He, J. Lu, Efficient removal of Bisphenol A in water via piezocatalytic degradation by equivalent-vanadium-doped SrTiO_3 nanofibers, *Chem. Eng. Sci.* 247 (2022), 116707.
- [26] H. Dong, Y. Zuo, N. Song, S. Hong, M. Xiao, D. Zhu, J. Sun, G. Chen, C. Li, Bimetallic synergetic regulating effect on electronic structure in cobalt/vanadium co-doped carbon nitride for boosting photocatalytic performance, *Appl. Catal. B: Environ.* 287 (2021), 119954.
- [27] H. Bantawal, U.S. Shenoy, D.K. Bhat, Vanadium doped CaTiO_3 cuboids: role of vanadium in improving the photocatalytic activity, *Nanoscale Adv.* 3 (2021) 5301–5311.
- [28] N.T.P. Le Chi, N.T. Dieu Cam, D. Van Thuan, T.T. Truong, N.T. Thanh Truc, C. Van Hoang, T.T. Thu Phuong, T.-D. Pham, M.H. Thanh Tung, N.T. Minh Thu, N. M. Phuong, V.N. Nguyen, Synthesis of vanadium doped tantalum oxy-nitride for photocatalytic reduction of carbon dioxide under visible light, *Appl. Surf. Sci.* (2019) 467–468, 1249–1255.
- [29] H. Bantawal, U.S. Shenoy, D.K. Bhat, Vanadium-Doped SrTiO_3 nanocubes: insight into role of vanadium in improving the photocatalytic activity, *Appl. Surf. Sci.* 513 (2020), 145858.
- [30] G. Li Puma, A. Brucato, Dimensionless analysis of slurry photocatalytic reactors using two-flux and six-flux radiation absorption–scattering models, *Catal. Today* 122 (2007) 78–90.
- [31] I. Grić, G. Li Puma, Six-flux absorption-scattering models for photocatalysis under wide-spectrum irradiation sources in annular and flat reactors using catalysts with different optical properties, *Appl. Catal. B: Environ.* 211 (2017) 222–234.
- [32] G. Kresse, J. Furthmüller, Efficient iterative schemes for ab initio total-energy calculations using a plane-wave basis set, *Phys. Rev. B* 54 (1996) 11169–11186.
- [33] J.P. Perdew, K. Burke, M. Ernzerhof, Generalized gradient approximation made simple, *Phys. Rev. Lett.* 77 (1996) 3865–3868.
- [34] G. Kresse, D. Joubert, From ultrasoft pseudopotentials to the projector augmented-wave method, *Phys. Rev. B* 59 (1999) 1758–1775.
- [35] P.E. Blöchl, Projector augmented-wave method, *Phys. Rev. B* 50 (1994) 17953–17979.
- [36] S. Grimme, J. Antony, S. Ehrlich, H. Krieg, A consistent and accurate ab initio parametrization of density functional dispersion correction (DFT-D) for the 94 elements H-Pu, *J. Chem. Phys.* 132 (2010), 154104.
- [37] Y. He, J. Qian, P. Wang, J. Wu, B. Lu, S. Tang, P. Gao, Acceleration of levofloxacin degradation by combination of multiple free radicals via MoS_2 anchored in manganese ferrite doped perovskite activated PMS under visible light, *Chem. Eng. J.* 431 (2022), 133933.
- [38] X. Li, J. Shi, X. Luo, Enhanced adsorption of rhodamine B from water by Fe-N co-modified biochar: preparation, performance, mechanism and reusability, *Bioresour. Technol.* 343 (2022), 126103.
- [39] J. Wu, J. Liu, B. Wen, Y. Li, B. Zhou, Z. Wang, S. Yang, R. Zhao, Nitrogen-rich covalent triazine frameworks for high-efficient removal of anion dyes and the synergistic adsorption of cationic dyes, *Chemosphere* 272 (2021), 129622.
- [40] J. Wu, X. Yan, L. Li, J. Gu, T. Zhang, L. Tian, X. Su, Z. Lin, High-efficiency adsorption of Cr(VI) and RhB by hierarchical porous carbon prepared from coal gangue, *Chemosphere* 275 (2021), 130008.
- [41] I. Benisti, R. Nandi, N. Amdursky, Y. Paz, Nanoseconds-resolved transient FTIR spectroscopy as a tool for studying the photocatalytic behavior of various types of bismuth vanadate, *Appl. Catal. B: Environ.* 278 (2020), 119351.
- [42] M.F.R. Samsudin, R. Bashiri, N.M. Mohamed, Y.H. Ng, S. Sufian, Tailoring the morphological structure of BiVO_4 photocatalyst for enhanced photoelectrochemical solar hydrogen production from natural lake water, *Appl. Surf. Sci.* 504 (2020), 144417.
- [43] M. Hajiali, M. Farhadian, S. Tangestaninejad, M. Khosravi, Synthesis and characterization of $\text{Bi}_2\text{MoO}_6/\text{MIL-101}(\text{Fe})$ as a novel composite with enhanced photocatalytic performance: effect of water matrix and reaction mechanism, *Adv. Powder Technol.* 33 (2022), 103546.
- [44] L. Zhang, J. Yang, T. Xie, S. Feng, L. Xu, Boosting visible-light-driven photocatalytic activity of BiPO_4 via constructing Schottky junction with $\text{Ti}_3\text{C}_2\text{MXene}$, *Mater. Des.* 192 (2020), 108772.
- [45] T. Xie, L. Xu, C. Liu, Y. Wang, Magnetic composite $\text{ZnFe}_2\text{O}_4/\text{SrFe}_{12}\text{O}_{19}$: preparation, characterization, and photocatalytic activity under visible light, *Appl. Surf. Sci.* 273 (2013) 684–691.
- [46] Y. Guo, Q. Zhou, J. Nan, W. Shi, F. Cui, Y. Zhu, Perylenetetracarboxylic acid nanosheets with internal electric fields and anisotropic charge migration for photocatalytic hydrogen evolution, *Nat. Commun.* 13 (2022) 2067.
- [47] X.L. Wang, J. Li, W.M. Liu, Synthesizing pyridinic-N dominate-doped graphene/ BiVO_4 nanocomposite as a superior photocatalyst for degradation under visible-irradiation, *Opt. Mater.* 114 (2021), 110922.
- [48] X. Xu, Y. Su, Y. Dong, X. Luo, S. Wang, W. Zhou, R. Li, K.P. Homewood, X. Xia, Y. Gao, X. Chen, Designing and fabricating a CdS QDs/ Bi_2MoO_6 monolayer S-

- scheme heterojunction for highly efficient photocatalytic C₂H₄ degradation under visible light, *J. Hazard. Mater.* 424 (2022), 127685.
- [49] X. Zhu, Z. Wang, K. Zhong, Q. Li, P. Ding, Z. Feng, J. Yang, Y. Du, Y. Song, Y. Hua, J. Yuan, Y. She, H. Li, H. Xu, Mo-O-Bi Bonds as interfacial electron transport bridges to fuel CO₂ photoreduction via in-situ reconstruction of black Bi₂MoO₆/BiO_{2-x} heterojunction, *Chem. Eng. J.* 429 (2022), 132204.
- [50] W. He, Y. Wei, J. Xiong, Z. Tang, Y. Wang, X. Wang, H. Xu, X. Zhang, X. Yu, Z. Zhao, J. Liu, Variable valence Mo⁵⁺/Mo⁶⁺ ionic bridge in hollow spherical g-C₃N₄/Bi₂MoO₆ catalysts for promoting selective visible light-driven CO₂ photoreduction into CO, *J. Energy Chem.* 80 (2023) 361–372.
- [51] Z. Xu, J. Jiang, M. Wang, J. Wang, Y. Tang, S. Li, J. Liu, Enhanced levofloxacin degradation by hierarchical porous Co₃O₄ with rich oxygen vacancies activating peroxymonosulfate: performance and mechanism, *Sep. Purif. Technol.* 304 (2023), 122055.
- [52] Y. Tang, Q. Liu, L. Dong, H.B. Wu, X.-Y. Yu, Activating the hydrogen evolution and overall water splitting performance of NiFe LDH by cation doping and plasma reduction, *Appl. Catal. B: Environ.* 266 (2020), 118627.
- [53] F. Wang, S.-S. Liu, Z. Feng, H. Fu, M. Wang, P. Wang, W. Liu, C.-C. Wang, High-efficient peroxymonosulfate activation for rapid atrazine degradation by Fe₃O₄@MoS₂ derived from MIL-88A(Fe), *J. Hazard. Mater.* 440 (2022), 129723.
- [54] J. Lu, Y. Zhou, Y. Zhou, Efficiently activate peroxymonosulfate by Fe₃O₄@MoS₂ for rapid degradation of sulfonamides, *Chem. Eng. J.* 422 (2021), 130126.
- [55] J. Yang, Q. Zhu, Z. Xie, Y. Wang, J. Wang, Y. Peng, Y. Fang, L. Deng, T. Xie, L. Xu, Enhancement mechanism of photocatalytic activity for MoS₂/Ti₃C₂ Schottky junction: experiment and DFT calculation, *J. Alloy. Compd.* 887 (2021), 161411.
- [56] X. Li, D. Wu, J. Yang, Q. Zhu, J. Wang, Y. Peng, T. Xie, H. Chen, Monoclinic BiPO₄: preparation, photocatalytic properties in experiment and theoretical calculation, *Sol. Energy* 220 (2021) 440–449.
- [57] J. Yang, T. Xie, Q. Zhu, J. Wang, L. Xu, C. Liu, Boosting the photocatalytic activity of BiOX under solar light via selective crystal facet growth, *J. Mater. Chem. C* 8 (2020) 2579–2588.
- [58] H. Huang, S. Tu, C. Zeng, T. Zhang, A.H. Reshak, Y. Zhang, Macroscopic polarization enhancement promoting photo- and piezoelectric-induced charge separation and molecular oxygen activation, *Angew. Chem. Int. Ed.* 56 (2017) 11860–11864.
- [59] J. Zhang, W. Zhao, Z. Li, G. Lu, M. Zhu, Visible-light-assisted peroxymonosulfate activation over Fe(II)/V(IV) self-doped FeVO₄ nanobelts with enhanced sulfamethoxazole degradation: Performance and mechanism, *Chem. Eng. J.* 403 (2021), 126384.
- [60] Y. Liu, W. Guo, H. Guo, X. Ren, Q. Xu, Cu (II)-doped V₂O₅ mediated persulfate activation for heterogeneous catalytic degradation of benzotriazole in aqueous solution, *Sep. Purif. Technol.* 230 (2020), 115848.
- [61] G. Zhang, H. Xu, J. Hu, Nanoarchitectonics on Bi₂MoO₆ by alkali etching for enhanced photocatalytic performance, *Adv. Powder Technol.* 32 (2021) 4384–4390.
- [62] J. Liqiang, Q. Yichun, W. Baiqi, L. Shudan, J. Baojiang, Y. Libin, F. Wei, F. Honggang, S. Jiazhong, Review of photoluminescence performance of nano-sized semiconductor materials and its relationships with photocatalytic activity, *Sol. Energy Mater. Sol. Cells* 90 (2006) 1773–1787.
- [63] X. Jiang, K. Xiao, Z. Liu, W. Xu, F. Liang, S. Mo, X. Wu, J. Beiyuan, Novel ⁰D–¹D–2D nanostructured MCN/NCDs recyclable composite for boosted peroxymonosulfate activation under visible light toward tetracycline degradation, *Sep. Purif. Technol.* 296 (2022), 121328.
- [64] D.L. Cocke, M.Y.A. Mollah, J.R. Parga, T.R. Hess, J.D. Ortego, An XPS and SEM/EDS characterization of leaching effects on lead- and zinc-doped portland cement, *J. Hazard. Mater.* 30 (1992) 83–95.
- [65] Q. Wang, Y. Zhao, J. Gao, H. Geng, J. Li, H. Jin, Triggering the reversible reaction of V³⁺/V⁴⁺/V⁵⁺ in Na₃V₂(PO₄)₃ by Cr³⁺ substitution, *ACS Appl. Mater. Interfaces* 12 (2020) 50315–50323.
- [66] G. Alnaggar, A. Hezam, Q.A. Drmash, S. Ananda, Sunlight-driven activation of peroxymonosulfate by microwave synthesized ternary MoO₃/Bi₂O₃/g-C₃N₄ heterostructures for boosting tetracycline hydrochloride degradation, *Chemosphere* 272 (2021), 129807.
- [67] Y. He, J. Qian, B. Xu, P. Wang, B. Lu, S. Tang, P. Gao, Encapsulate SrCoO₃ perovskite crystal within molybdenum disulfide layer as core-shell structure to enhance electron transfer for peroxymonosulfate activation, *Sep. Purif. Technol.* 283 (2022), 120199.